

# Depth-dependent global properties of a sunspot observed by Hinode (SOT/SP)

Sanjiv K. Tiwari<sup>1,2</sup>, Michiel van Noort<sup>1</sup>, Sami K. Solanki<sup>1,3</sup>, Andreas Lagg<sup>1</sup>

<sup>1</sup>Max-Planck-Institut für Sonnensystemforschung, Justus-von-Liebig-Weg 3, 37077 Göttingen, Germany.

<sup>2</sup>NASA Marshall Space Flight Center, ZP 13, Huntsville, AL 35812, USA.

<sup>3</sup>School of Space Research, Kyung Hee University, Yongin, Gyeonggi 446-701, Republic of Korea.  
e-mail: [tiwari;vannoort;solanki;lagg]@mps.mpg.de

Preprint online version: October 6, 2018

## ABSTRACT

**Context.** The three dimensional structure of sunspots has been extensively studied for the last two decades. A recent advancement of the Stokes inversion technique prompts us to revisit the problem.

**Aims.** In the present work, we aim to investigate the global depth-dependent thermal, velocity and magnetic properties of a sunspot, as well as the interconnection between various local properties.

**Methods.** High quality Stokes profiles of the disk centered, regular, leading sunspot of NOAA AR 10933 acquired by the Solar Optical Telescope/Spectropolarimeter onboard the Hinode spacecraft are analyzed. To obtain the depth-dependent stratification of the physical parameters, we have utilized the recently developed spatially coupled version of the SPINOR inversion code.

**Results.** We first study the azimuthally averaged physical parameters of the sunspot. The vertical temperature gradient in the lower to mid-photosphere is smallest in the umbra, it is considerably larger in the penumbra and still somewhat larger in the spot's surroundings. The azimuthally averaged field becomes more horizontal with radial distance from the center of the spot, but more vertical with height. At continuum optical depth unity, the line-of-sight velocity shows an average upflow of  $\sim 300 \text{ ms}^{-1}$  in the inner penumbra and an average downflow of  $\sim 1300 \text{ ms}^{-1}$  in the outer penumbra. The downflow continues outside the visible penumbral boundary. The sunspot shows at most a moderate negative twist of  $< 5^\circ$  at  $\log(\tau) = 0$ , which increases with height. The sunspot umbra and the spines of the penumbra show considerable similarity in their physical properties albeit with some quantitative differences (weaker, somewhat more horizontal fields in spines, commensurate with their location further away from the sunspot's core). The temperature shows a general anticorrelation with the field strength, with the exception of the heads of penumbral filaments, where a weak positive correlation is found. The dependence of the physical parameters on each other over the full sunspot shows a qualitative similarity to that of a standard penumbral filament and its surrounding spines.

**Conclusions.** The large-scale variation of the physical parameters of a sunspot at various optical depths is presented. Our results suggest that the spines in the penumbra are basically the outward extension of the umbra. The spines and the penumbral filaments are together the basic elements forming a sunspot penumbra.

**Key words.** Sun: magnetic fields – Sun: photosphere – Sun: sunspots

## 1. Introduction

High-resolution observations of sunspots, dark features on the solar surface, reveal that they contain small-scale, dynamically evolving structures, such as umbral dots (Danielson 1964; Riethmüller et al. 2008, 2013), light bridges (Sobotka et al. 1997; Rimmele 2008; Shimizu 2011; Lagg et al. 2014), spines (Lites et al. 1993), penumbral filaments (Tiwari et al. 2013, and references therein), and concentrated strong downflows at spot's periphery (van Noort et al. 2013). In spite of the fast dynamical evolution of these elementary features ( $\sim 10$  minutes to 4 hours, see, e.g., Sobotka 1997; Solanki & Rüedi 2003), the sunspots themselves are long-lasting, from days to months, and evolve only slowly. To understand this relative stability, it is essential to study the global properties of sunspots, in addition to exploring their fine-scale structure. Global

properties of sunspots are also of interest as constraints for global spot models, for studies of active region magnetic fields and associated activity, for investigations of solar irradiance variations and as proxies for starspots.

In the last two decades, considerable advances have been made in understanding the three dimensional (3D) sunspot structure in the solar atmosphere both theoretically (Rempel et al. 2009a,b; Rempel & Schlichenmaier 2011; Rempel 2012) and observationally (Solanki et al. 1992; Lites et al. 1993; Title et al. 1993; Stanchfield et al. 1997; Westendorp Plaza et al. 1998, 2001b,a; Solanki 2003; Mathew et al. 2003; Borrero & Ichimoto 2011). Many of the depth-dependent global properties of the magnetic, thermal and velocity fields in sunspots are verified by the above researchers. For example, within sunspots, the magnetic field strength increases, whereas field inclination decreases with depth in general, temperature increases with both depth and radius, and the line-of-sight velocity shows

Send offprint requests to: S. K. Tiwari e-mail: sanjiv.k.tiwari@nasa.gov

net upflows and downflows in the inner and outer penumbra, respectively.

When looked at in detail, the more vertical fields in the penumbra (spines: according to Lites et al. 1993) were found to be stronger than their surroundings. However, their thermal structure remained controversial. Wiehr (2000) associated dark penumbral features with the stronger and more horizontal fields. Similar to Westendorp Plaza et al. (2001b), Langhans et al. (2005) found the stronger penumbral magnetic field to be more vertical and brighter. Borrero & Ichimoto (2011) found more horizontal fields (intra-spines) weaker and brighter in the inner penumbra and darker in the outer penumbra (see Solanki 2003, for a detailed review of earlier literature). Such controversies were recently addressed by Tiwari et al. (2013), who showed that the heads of sunspot penumbral filaments are brighter and contain vertical magnetic field, whereas their tails are darker and contain oppositely directed, strong, vertical magnetic field. Only the darker regions with less inclined to the vertical fields of the same polarity as the umbra can be associated with the spines. It was also confirmed that the magnetic field in the spines wraps around the intra-spines in higher layers, as expected from the models of Solanki & Montavon (1993) and Spruit & Scharmer (2006), and reported by Borrero et al. (2008).

However, many issues are yet to be resolved. E.g., the magnetic canopy structure, which is a result of the expansion of the magnetic field, is not unambiguously observed and understood. Westendorp Plaza et al. (2001b); Rezaei et al. (2006) and Borrero & Ichimoto (2011) found that the canopy starts well within the sunspot penumbra and continues outside of it, whereas Mathew et al. (2003) did not find a magnetic canopy structure anywhere. Balthasar & Gömöry (2008) found canopy only outside the penumbral boundary in contrast to the abovementioned researchers, but in agreement with, e.g., Giovanelli (1980); Giovanelli & Jones (1982); Solanki et al. (1992, 1994, 1999); Adams et al. (1993).

Similarly, the relationship between the temperature and magnetic field strength over the full sunspot is not fully understood (Solanki 2003). A non linear relationship between temperature (and/or intensity) and magnetic field is observed by Solanki et al. (1993); Mathew et al. (2004), which is in agreement with the anticorrelation found by other researchers, e.g., Kopp & Rabin (1992); Martínez Pillet & Vázquez (1993); Stanchfield et al. (1997). The above authors attributed the non-linearity in the (penumbral) lower temperature part of their scatter plots to the outer penumbral features. However, the different parts of the non-linearity in the scatter plots between  $B$  and  $T$ , e.g., a nearly constant temperature (of  $\sim 5800$ – $5900$  K) for a range of magnetic field strength (0–2500 G) found by Westendorp Plaza et al. (2001b), remained unexplained.

The magnetic field strength and inclination are anti-correlated, with more vertical fields having higher field strength (e.g. Stanchfield et al. 1997; Westendorp Plaza et al. 2001b). This relationship mirrors the large-scale structure of sunspots. At smaller scales we expect a relationship affected by the local magnetoconvective structure, with strong opposite polarity fields at the tails of the penumbral filaments

(Tiwari et al. 2013), see also Scharmer et al. (2013) and Ruiz Cobo & Asensio Ramos (2013).

The source of the Evershed flow (Evershed 1909) is near the heads of penumbral filaments, the gas cools down while it travels the bulk of the filaments and sinks as cool material at the tails of the filaments (Tiwari et al. 2013). Thus, a clear systematic relationship between temperature and line-of-sight velocity was found by Tiwari et al. (2013) for a standard penumbral filament, in that the upflows were hotter and the downflows were cooler. How this pattern, together with the cool spines, affects the structure of the full sunspot would be an interesting extension.

In spite of the large number of works on global sunspot properties (see references above, and e.g., Lites et al. 1993; Westendorp Plaza et al. 2001b,a; Solanki 2003; Mathew et al. 2003; Tritschler et al. 2004; Bellot Rubio et al. 2004; Borrero & Ichimoto 2011), a description of these properties in terms of elementary, small-scale structures, such as umbral dots, spines, penumbral filaments, etc., has thus far not been given.

Recent advances in the inversion of the high quality spectro-polarimetric observations from SOT/SP provide us with an opportunity to take a fresh look at the abovementioned issues in detail. In the present paper, we analyze the results of a depth-dependent inversion of a full sunspot and surrounding region. The same inverted results are analyzed as done earlier by Tiwari et al. (2013). Whereas in that paper we concentrated mainly on the internal structure of penumbral filaments, here we focus on the global and partly local properties of the inverted sunspot.

The paper is organized as follows. Details of the observations and the inversion process are given in the next section. In Section 3, we present the depth-dependent global thermal, velocity and magnetic properties of the sunspot. Mutual dependence of physical parameters, and inferred substructures of the sunspot are given in Section 4. In Section 5, we discuss our results, and finally, in Section 6, we present our conclusions.

## 2. Observations and inversion

We have used a high spatial resolution spectro-polarimetric scan of the leading sunspot of the active region (AR) NOAA 10933, recorded by the Solar Optical Telescope/Spectropolarimeter (SOT/SP: Tsuneta et al. 2008; Suematsu et al. 2008; Ichimoto et al. 2008; Shimizu et al. 2008) onboard the Hinode satellite (Kosugi et al. 2007). The positive polarity spot of the NOAA AR 10933 that we use in the present study was observed close to the solar disk center ( $\mu=0.99$ ) on the 5<sup>th</sup> of January 2007 from 12:36 to 13:10 UT. The atomic lines contained in the data are the Fe I lines at 6301.5 and 6302.5 Å. The SP scans are acquired in “normal mode” of SOT, with a spatial sampling of  $0.16''\text{pixel}^{-1}$ .

We perform the calibration of the Hinode (SOT/SP) data by using the standard “SP\_PREP” routine, developed by B. Lites, which is available in the Solar Software package. The “SP\_PREP” routine computes the thermal shifts in the spectral and slit dimensions first, and then applies the drift corrections for calibrating the data from level 0 to level 1 (Lites & Ichimoto 2013).

The observed continuum intensity map of the inverted region is shown in Fig. 1. The spot has an average diameter of about  $50''$ , and different aspects of

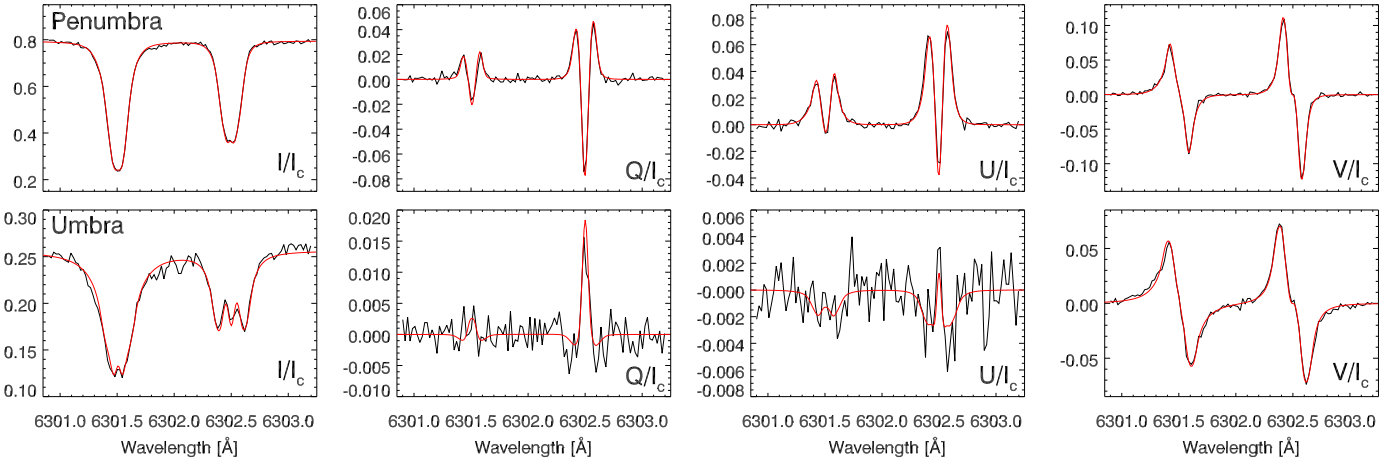


**Fig. 2.** Examples of observed (black) and best-fit (red) Stokes profiles: I, Q, U and V. Upper row displays Stokes profiles for a typical pixel in the sunspot penumbra (location: X48'', Y41.6''). Lower row contains Stokes profiles for one of the darkest pixels in the sunspot umbra (location: X36'', Y32'').

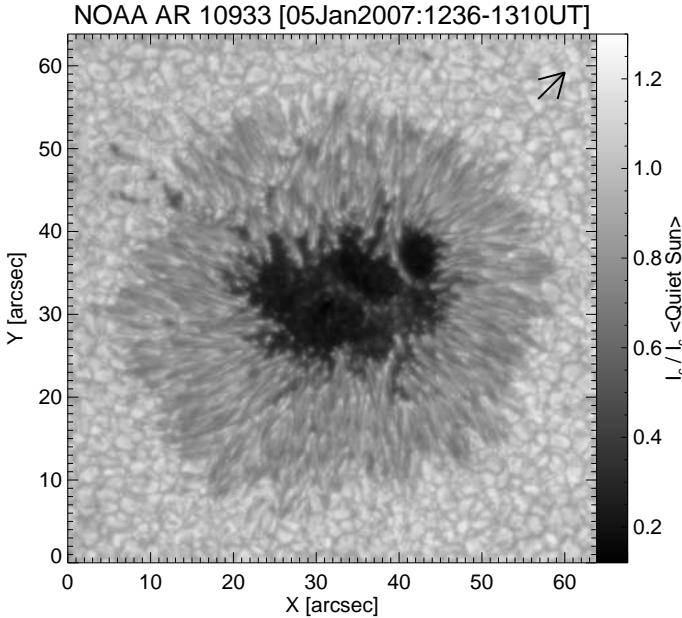


**Fig. 1.** Continuum intensity map of the sunspot NOAA AR 10933, observed by Hinode in normal scan mode of SOT/SP on 05 January 2007 between 12:36 and 13:10 UT. The arrow indicates the direction of the solar disk center.

it have been already studied in a number of publications, see, e.g., Kubo et al. (2008); Tiwari et al. (2009); Franz & Schlichenmaier (2009); Venkatakrishnan & Tiwari (2009, 2010); Katsukawa & Jurčák (2010); Franz (2011); Borrero & Ichimoto (2011); Tiwari (2012); Riethmüller et al. (2013); van Noort et al. (2013); Tiwari et al. (2013).

### 2.1. Inversion

We employ the output of the SPINOR inversion code (Frutiger et al. 2000; Frutiger 2000) in the spatially coupled mode (van Noort 2012; van Noort et al. 2013) used by Tiwari et al. (2013) to invert the calibrated Stokes profiles. The SPINOR code builds on the STOPRO line synthesis routines by Solanki (1987) and solves the radiative

transfer equations numerically under the assumption of local thermodynamical equilibrium (LTE). The spatially coupled version of the SPINOR inversion code employs a modified Levenberg–Marquardt (L–M) algorithm for the optimization of a simplified, height-dependent atmospheric model, simultaneously over an extended field-of-view, taking into account the spatial degradation caused by the telescope. The required spectro-polarimetric derivatives with respect to the fitted atmospheric structure, required by the L–M algorithm, are calculated using response functions (Landi Degl’Innocenti & Landi Degl’Innocenti 1977; Ruiz Cobo & del Toro Iniesta 1992). To resolve the maximum amount of spatial structure, a Fourier interpolation of the data was made to allow the inversion to be carried out at an increased spatial sampling by a factor of two (van Noort et al. 2013). Thus, the pixel size for resultant physical parameters used in the study is 0.08''.

The vertical structure of the temperature  $T$ , magnetic field strength  $B$ , inclination  $\gamma$ , azimuth  $\chi$ , line-of-sight velocity  $v_{\text{LOS}}$ , and microturbulent velocity  $v_{\text{mic}}$  are approximated using bicubic splines, controlled by 3 nodes, placed at  $\log(\tau) = -2.5, -0.9$  and  $0$ , where  $\tau$  is the continuum optical depth at  $\lambda = 6302.5 \text{ \AA}$ .

To aid in the convergence of the solution, every 10 iterations, all slowly converging pixels were re-initialized using the nearest neighbours, and the whole solution was then smoothed over by convolution with a Gaussian smoothing function, which significantly speeds up convergence if appropriate selection criteria for re-initialization are used. Although it is possible that this procedure creates a preference for a spatially smooth solution, it clearly results in a significant increase of the fit quality, i.e., a reduction of the difference between squared of the data and the fitted profiles. While, as in all inversions, the adopted solution may or may not represent the global optimum, it does appear to represent a workable optimum, since additional attempts to disturb and re-converge the solution did not significantly increase the accuracy of the fit, and resulted in a very similar solution.

Examples of observed and fitted Stokes profiles for a typical pixel each from penumbra and umbra are shown in Fig 2. The atomic parameters used in the inversion are 6302.4936:  $\log(gf) = -1.203$ ,  $E_l = 3.6866 \text{ eV}$ , and 6301.5012:



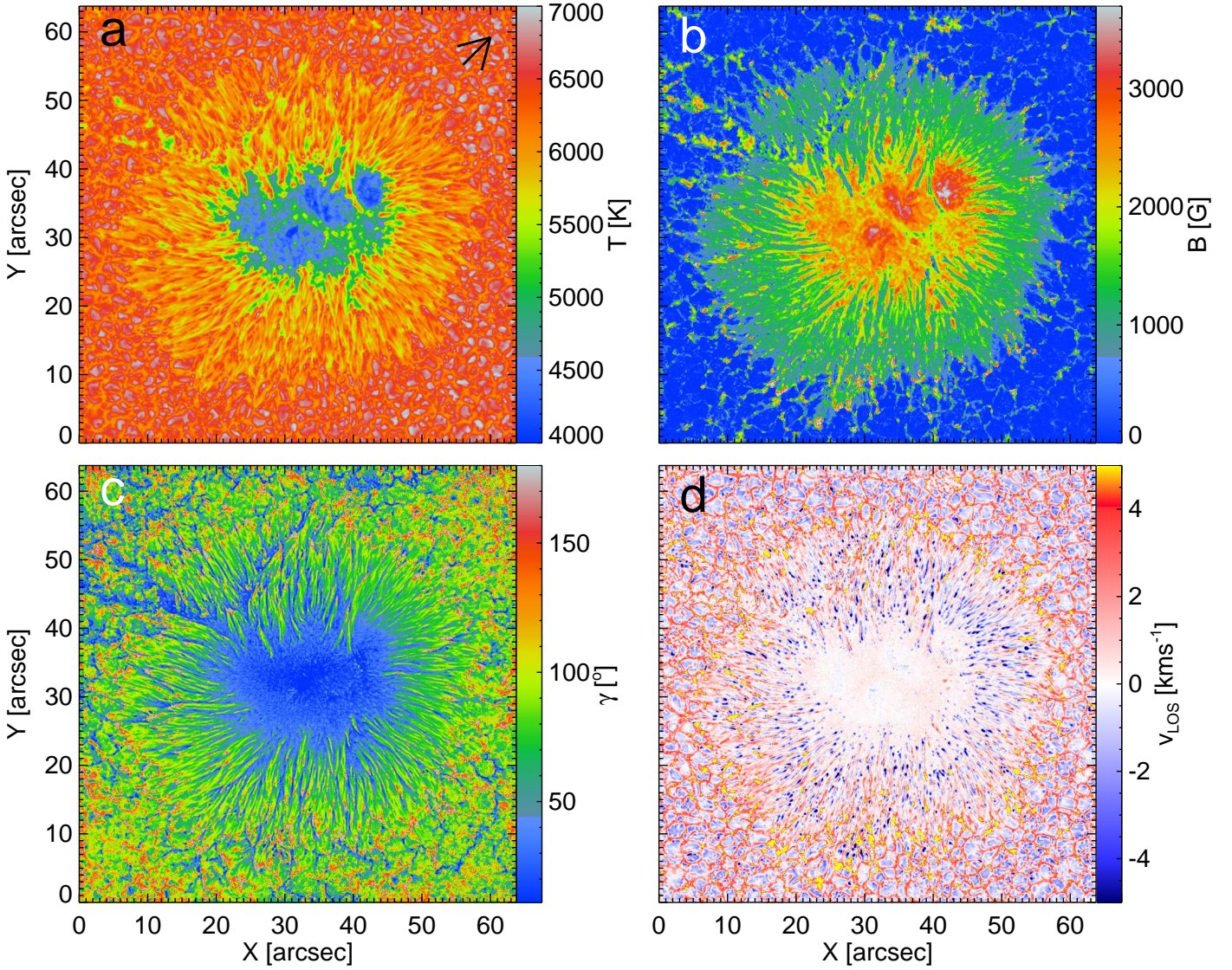


**Fig. 3.** Maps of selected physical parameters (at  $\log(\tau) = 0$ ) obtained from the inversion: (a) temperature  $T$ , (b) magnetic field strength  $B$ , (c) magnetic field inclination  $\gamma$ , (d) line-of-sight velocity  $v_{\text{LOS}}$ . The arrow in the temperature map points to solar disk center. Except for field inclination  $\gamma$ , thresholds have been used for minimum and maximum values of colorbars. The extreme values returned by the inversion are 3853 to 7173 K for  $T$ , 10 to 4000 G for  $B$ , and  $-11.5$  to  $18.7 \text{ km s}^{-1}$  for  $v_{\text{LOS}}$ .

$\log(gf) = -0.745$ ,  $E_I = 3.6539 \text{ eV}$ . Collisional broadening was calculated using the ABO tables (Barklem et al. 1998). Fe I abundance was set to 7.50. Please note that no molecular lines are included in the inversion since it makes the inversion process extremely slow. This sunspot was not particularly cool, so that the inversion seems not to be severely affected by contamination through molecular lines (see, e.g., example fits for one of the darkest pixels in the sunspot umbra in Fig. 2).

A test performed by van Noort et al. (2013) to establish the robustness of the inversion by changing the node positions and by adding different levels of noise in the observed and convolved profiles resulted in very similar inverted quantities, thus suggesting that the inversion result is reliable. Moreover, van Noort (2012); van Noort et al. (2013) find a good agreement between the inversion results and 3D radiation magnetohydrodynamics (MHD) simulations with the MURAM code (Vögler et al. 2005) for the

velocities and fields, providing further support on the reliability of our inversion process. This result is supported by the fact that for most pixels the response functions are non-zero for all three chosen nodes, importantly including the one at  $\log(\tau) = 0$ .

However, establishing the error in the fitted atmospheric parameters is a tedious task due to the spatial coupling of the parameters. A change introduced in a parameter at one pixel will cause the code to adjust the fit of that and other parameters in the neighboring pixels. Therefore, to properly determine the error in the fitted parameters, a perturbation of each parameter at every pixel, followed by a full re-conversion of the inversion in all other pixels is required, requiring a prohibitively large amount of computational power.

The wavelength calibration of the data was carried out by requiring that the umbra of the sunspot, excluding the umbral dots, was on average at rest at  $\tau = 1$ . This resulted



in a small systematic correction of the line-of-sight velocity,  $v_{\text{LOS}}$ , of  $100 \text{ m s}^{-1}$ , which was subtracted from the inversion results presented here.

The  $180^\circ$  azimuthal ambiguity was resolved after the inversion by using the minimum energy method (Metcalf 1994; Leka et al. 2009).

In Fig. 3, we display full maps of inversion results of some of the physical parameters (fitted temperature  $T$ , magnetic field strength  $B$ , field inclination  $\gamma$  and line-of-sight velocity  $v_{\text{LOS}}$ ) at  $\log(\tau) = 0$ . The physical parameters look smooth, in addition to having high contrast (e.g., compare the observed continuum intensity from Fig. 1 with the one obtained from the inversion, shown in Fig. 4, discussed later). At  $\log(\tau) = -0.9$ , where the response of the spectral lines 6301.5 and 6302.5 Å to most of the physical parameters is largest, the physical parameters become smoother than at  $\log(\tau) = 0$ .

### 3. Global properties

To investigate the global properties of the sunspot, we selected several contours of magnetic field strength of the spot, which was first smoothed by a factor of about twenty ( $20 \times 20$  pixels) in order to get smooth contours. Outer contours required smoothing by even larger factors (up to 50) due to more fluctuations along the azimuthal path present there. Ten contours out of a total of 21 are shown in red in Fig. 4. The inner and outer penumbral boundaries are determined on the basis of intensity, and are indicated by the yellow contours in Fig. 4.

We note that the outermost red contour and the outer yellow one differ quite significantly at some places. This has partly to do with the different amount of smoothing applied to the field strength and continuum intensity prior to determining the contours, but partly also with a mismatch between field strength and intensity near the penumbral boundary. We carefully looked at these regions and found that many of them are the tails of penumbral filaments with high-speed downflows and contain very strong fields with a polarity opposite to that of the sunspot umbra (van Noort et al. 2013). In most of these regions the tails of several penumbral filaments seem to converge. The most prominent excursion of the outermost red contour beyond the yellow contour ( $X \approx 10''$ ,  $Y \approx 45''$ ) is in the direction of a group of same polarity pores i.e., in a direction in which the penumbra is strongly distorted.

#### 3.1. Thermal properties

To explore the variation of the continuum intensity and temperature along the radius of the sunspot, we averaged these parameters azimuthally along the given contours (at the three optical depth positions for temperature, corresponding to the nodes used for the vertical spline interpolation of the atmosphere). The mean values, along with the root mean square (RMS) variation of the sample along the path of the contours (not to be confused with the standard error to the mean), are plotted in Fig. 5. The RMS variations are quite large, indicating the presence of fine-scale structures along the path of the contours. Please note that the contours are based on the magnetic field strength and are not equidistant, therefore the corresponding error bars are also not equidistant.

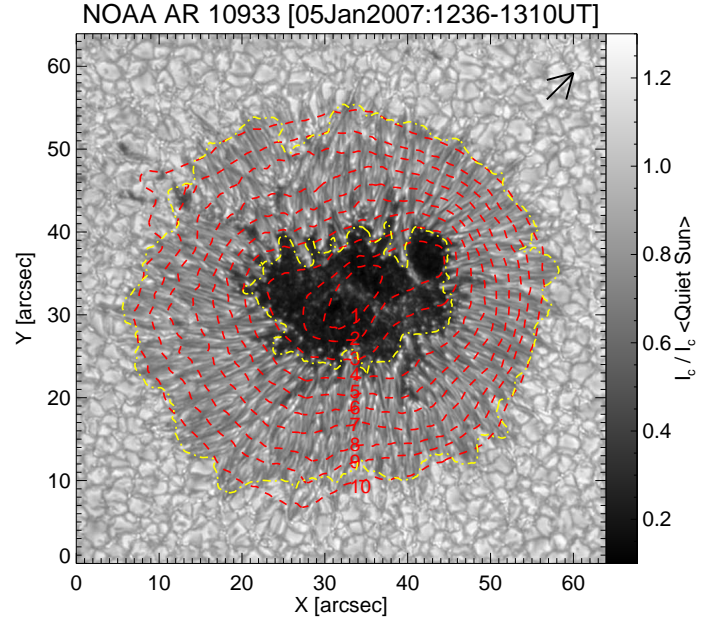


**Fig. 4.** Ten of the 21 contours of magnetic field strength over-plotted on the inverted continuum intensity map. Red contours are based on the smoothed magnetic field strength. Yellow contours are based on the intensity and represent the boundaries of the sunspot penumbra. The grey-scale bar ranges from 0.1 to 1.3; the extreme values of  $I_c/I_c < \text{Quiet Sun} >$  returned from the inversion are 0.097 and 1.468. The black arrow on the upper right part of the image points towards solar disk center.

The brightness of the umbra increases with radial distance from the center of the spot. We find the umbra to have an azimuthally averaged intensity of 20-40% of the quiet Sun in the continuum at 6302.0 Å, in agreement with earlier findings (e.g., Westendorp Plaza et al. 2001b). Note that the darkest part of the umbra has continuum intensities as low as 10% of the quiet Sun. The penumbra has a brightness of 45-85% of that of the averaged quiet Sun. Please note, however, that these values depend on the criterion used to determine the umbra-penumbral boundary and on the wavelength, see e.g., Mathew et al. (2003) for infrared wavelengths. They also depend on the size of sunspots (Mathew et al. 2007, and references therein), whereas the purported dependence on the phase of solar cycle remains inconclusive (Albregtsen & Maltby 1978, 1981; Albregtsen et al. 1984; Maltby et al. 1986; Norton & Gilman 2004; Penn & Livingston 2006; Mathew et al. 2007).

The behavior of the azimuthally averaged temperature at the deepest node  $\log(\tau) = 0$ , shown in the lower panel of Fig. 5, mimics that of the continuum intensity, displayed in the upper panel of the same figure, closely. This is as expected for an LTE inversion result. The temperature drops more rapidly from penumbra to umbra in the deeper layers than higher up, suggestive of a smaller vertical temperature gradient in the spot. Whereas in the penumbra this vertical temperature gradient is only slightly smaller than that in the quiet Sun, it is much smaller in the umbra. This latter result is in good agreement with the literature (see e.g., Schröter 1971; Maltby et al.

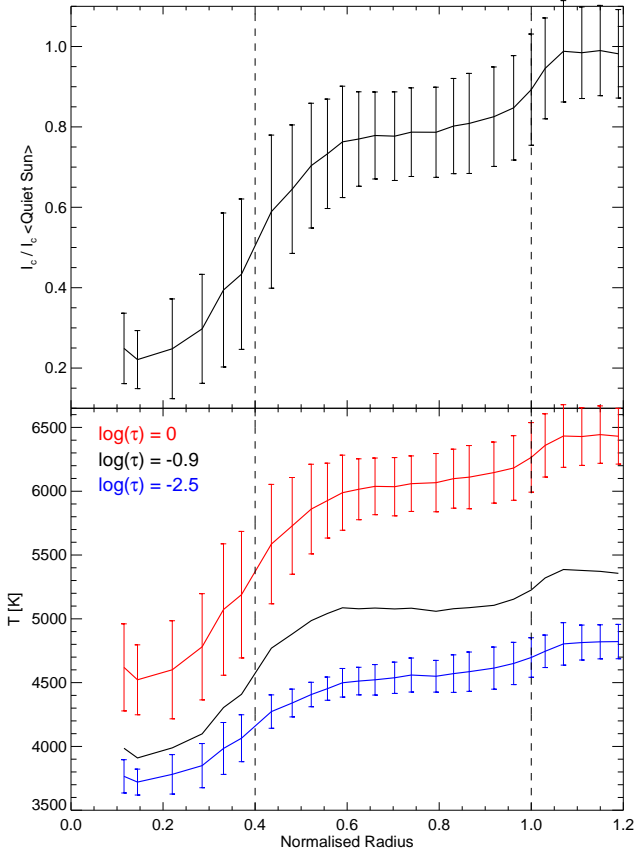


**Fig. 5.** Upper panel: Radial distribution of the azimuthally averaged continuum intensity normalised to averaged quiet Sun. The error bars represent the RMS variation along the azimuthal path of the contours. Lower panel: Radial dependence of the azimuthal averages of temperature at three optical depth positions. The two vertical dashed lines represent average radial positions of the boundaries of the sunspot penumbra.

1986; Collados et al. 1987; Westendorp Plaza et al. 2001b; Solanki 2003; Tritschler et al. 2004).

The temperature shows the largest fluctuations at  $\log(\tau) = 0$ . Since the temperature is very well constrained in this layer, largely by the continuum intensity, such strong fluctuations are an intrinsic property of the sunspot atmosphere, caused by fine-scale structures present therein.

### 3.2. Velocity stratification

Our sunspot was located almost at the center of the solar disk (within  $5^\circ$ ), allowing us to treat the line-of-sight (LOS) velocity as the vertical velocity, and to ignore projection effects. We find that the deepest layer in the inner penumbra is dominated by upflows (see Fig. 3d), in agreement with earlier findings. This is as expected from the dominating presence, in this location of the spot, of heads of penumbral filaments containing strong upflows (Tiwari et al. 2013). At the outer boundary of the sunspot penumbra, strong downflows dominate in the deepest layer, again as expected from the known concentrations, at this location, of the tails of penumbral filaments with strong downflows (van Noort et al. 2013; Tiwari et al. 2013). This large-scale radial structure of flows was seen

earlier by Rimmele (1995a); Schlichenmaier & Schmidt (2000); Westendorp Plaza et al. (2001a); Tritschler et al. (2004); Rimmele & Marino (2006); Ichimoto et al. (2007a); Sánchez Almeida et al. (2007); Franz & Schlichenmaier (2009).

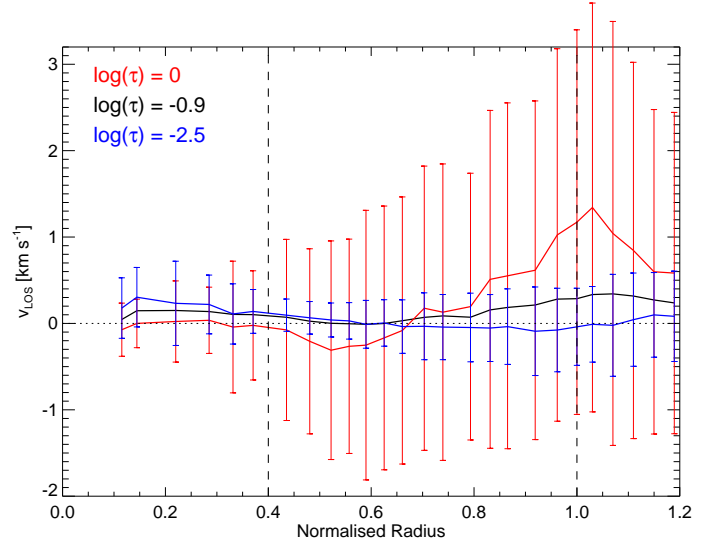


**Fig. 6.** Azimuthal averages of  $v_{\text{LOS}}$  at three optical depths plotted vs. normalized radial distance from center of the spot (solid lines). The RMS variations along each azimuthal contour are indicated for  $\log(\tau) = 0$  and  $-2.5$  by the red and blue vertical bars, respectively. The two vertical dashed lines have the same meaning as in Fig. 5.

In Fig. 6, we present the azimuthally averaged  $v_{\text{LOS}}$  at the three depth node positions vs. radius. This plot clearly shows the domination of upflows in the inner penumbra, with the average velocity in the deepest layer at around  $-300 \text{ m s}^{-1}$ , and the even greater domination of downflows in the outer penumbra with the average velocity reaching values as high as  $1300 \text{ m s}^{-1}$  just outside the sunspot boundary. The rapid increase of the RMS variations with depth is in good agreement with results of studies considering the fine structure of penumbrae (see e.g., Tiwari et al. 2013, and references therein). The RMS fluctuations also increase nearly linearly with radial distance until the outer boundary of the spot, indicating increased inhomogeneity in the vertical velocity.

The average downflow in the deepest layer increases in strength up to a normalized radius of  $\sim 1.05$ , outside the visible boundary of the sunspot. The increase of the velocity beyond the boundary of the spot comes from the fact that some of the strongest downflowing regions are not inside the contour marking the sunspot boundary, as pointed out in the beginning of Section 3. Furthermore, the downflows continue well beyond the boundary of the sunspot in agreement with Böerner & Kneer (1992).

The average velocity in the umbra is zero at  $\log(\tau) = 0$ , which was set by the velocity calibration described in the Section 2.1. The average velocity in the higher layers of the umbra remains close to (but different from) zero throughout the sunspot. In particular, there is a systematic weak downflow in the umbra above  $\log(\tau) = 0$ , which increases with height, although, as we will discuss in Section 5.1, the reliability of this result remains unclear.

The average velocity in the penumbra is a significant downflow of about  $350 \text{ m s}^{-1}$  at  $\log(\tau) = 0$ , as expected from the presence of strong downflows at the outer boundary of the penumbra. This average downflow decreases with height reaching to zero at  $\log(\tau) = -2.5$ .

### 3.3. Magnetic properties

#### 3.3.1. Azimuthal averages of field strength, $B$ , and inclination, $\gamma$

Azimuthally averaged values of  $B$  and  $\gamma$ , along with their RMS variations along the contours, are plotted in Fig. 7. Note that the large RMS variations are again indicative of the presence of fine-scale structures along the path of the contours, although in the umbra the RMS variations rather indicate the larger-scale inhomogeneity of  $B$  and  $\gamma$ . The lower values of the error bars go below zero for the field strength because the distribution of the field strength along the path of those contours departs significantly from a Gaussian.

We can see that the average magnetic field strength decreases nearly linearly with radial distance from the center of the spot. The drop in field strength at  $\log(\tau) = 0$ , from 2800 G (in umbra) to 700 G (at outer penumbral boundary), is slightly larger than at the other two heights. Also noticeable is the substantial weakening of the field strength in the two lowest nodes outside the sunspot boundary.

The general trend of decrease in the field strength with increasing radius is similar to that observed by Westendorp Plaza et al. (2001b); Mathew et al. (2003), and Borrero & Ichimoto (2011), but the height dependence of  $B$  in our plots, as discussed later, does not match either with that of Westendorp Plaza et al. (2001b), and Borrero & Ichimoto (2011), or with that of Mathew et al. (2003).

Fig. 7 shows that there are two regions where the azimuthally averaged magnetic field strength increases with height: just outside the visible boundary of the sunspot penumbra and in the region between radial positions 0.43 and 0.63. These are the locations of canopy structure and positive field gradient, respectively, which we describe in the next section (3.3.2).

The azimuthally averaged field inclination increases with radius, in agreement with the behavior of an expanding flux tube. The averaged magnetic field inclination consistently exhibits more vertical fields in the higher layers in the umbra and penumbra. The magnitude of this vertical gradient,  $5\text{--}10^\circ$  between the lower and middle photosphere is sizable. Outside the sunspot, however, the field in the deepest layer becomes more vertical and azimuthal averages of inclinations at all the three heights are nearly the same.

The fluctuations in both the field strength and inclination are largest in the deepest layer, and those in the inclination increase towards the outer boundary of the sunspot.

#### 3.3.2. Field gradients and canopy structure

To estimate the magnetic field gradient, one needs to obtain the field strength on a geometrical height ( $z$ -) scale, whereas the inversion code delivers the stratification of each physical parameter on a continuum optical depth ( $\tau$ -) scale. The transformation of optical depth scale to geometrical

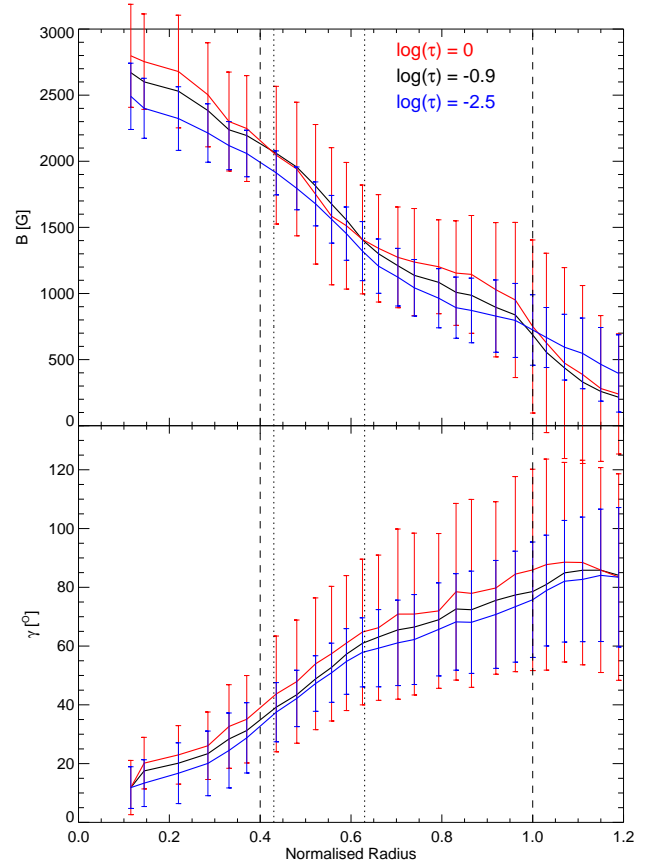


**Fig. 7.** Azimuthal averages of  $B$  (upper panel) and  $\gamma$  (lower panel) along the sunspot radius at three optical depths. Also shown are RMS variations for the uppermost and lowermost node positions (blue and red error bars, respectively). The two vertical dashed lines represent the inner and outer boundaries of the sunspot penumbra (on average). The two dotted lines outline the radius between which a positive field gradient is seen (i.e., field strength increasing upward).

height is not straight forward because of the unknown optical corrugation of the surface over sunspots. We carried out this transformation by assuming hydrostatic equilibrium. We are well aware that this is a gross simplification since it neglects the influence of the magnetic field; see also Puschmann et al. (2010).

The average vertical field gradient  $\partial B / \partial z$  in the sunspot umbra near the deepest node, where the highest field strength is about 4000 G, was determined to be  $-1.4 \text{ G km}^{-1}$ . The gradient becomes smaller with height and reaches a value of  $-0.95 \text{ G km}^{-1}$  at  $\log(\tau) = -2.5$ . The magnitude of the field gradient found for our sunspot is equivalent to that found in 3D magnetohydrodynamic (MHD) simulations ( $-1.5 \text{ G km}^{-1}$  for a sunspot whose strongest magnetic field is close to 4000 G at  $\tau = 1$ : M. Rempel, 2013, private communication).

The azimuthally averaged magnetic field shows a positive gradient (opposite to that seen in the umbra) in the inner-middle part of the penumbra (roughly between radius = 0.43 and 0.63), and just outside the sunspot (see upper panel of Fig. 7). The positive gradient observed outside the sunspot penumbra can clearly be associated with the magnetic canopy structure



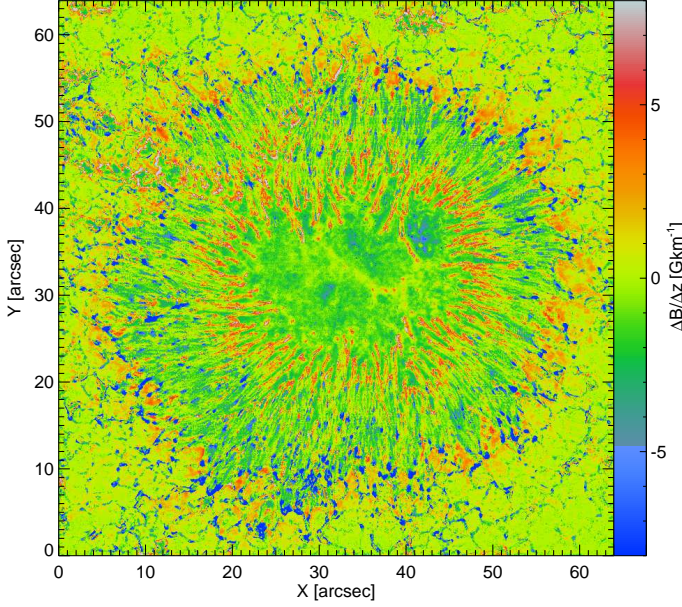


**Fig. 8.** Gradient of magnetic field computed between the geometrical height corresponding to the two deepest nodes ( $\log(\tau) = -0.9, 0$ ). A positive field gradient represents field strength increasing with height.

(Giovanelli 1980; Giovanelli & Jones 1982; Solanki et al. 1992; Solanki & Schmidt 1993; Solanki et al. 1994, 1999), whereas the inverse gradient seen in the inner-middle part of the penumbra in the deepest layers must have a different source. Fig. 8 clearly reveals the locations of the positive field strength gradient present in the inner-middle penumbra and at the outer penumbral boundary. Such an inverse gradient is also seen in Vacuum Tower Telescope (VTT: Schroeter et al. 1985) data by Joshi et al. (2015), see, Joshi (2014), who analyzed this particular property of the sunspots in detail. They have found such positive gradients also to be present in the inner penumbrae of MHD simulations of sunspots.

Although locally a positive field gradient is clearly visible between the optical depth layers  $\log(\tau) = -0.9$ , and 0, this is not the case for the azimuthal averages outside the spot, where the negative gradient contributions dominate over the positive ones. Only in the upper node is the average field strength larger than in the deepest layer (see, upper panel of Fig. 7).

The strongest negative field gradients concentrated locally near the outer spot boundary (see, Fig. 8) are found to be associated with strong downflows having the opposite polarity to the umbra. The very strong field strength in these regions in the deepest magnetic layers (some of them reaching up to 4 kG, the value set a priori as an upper limit in the inversion) can probably explain the strong negative field gradients seen at these locations (see, e.g., van Noort et al. 2013, for details).

### 3.3.3. Field azimuth and twist in the sunspot

A field azimuth map obtained at the middle node ( $\log \tau = -0.9$ ) is shown in the left panel of Fig. 9. It displays a generally radially directed field, with considerable small-scale structure.

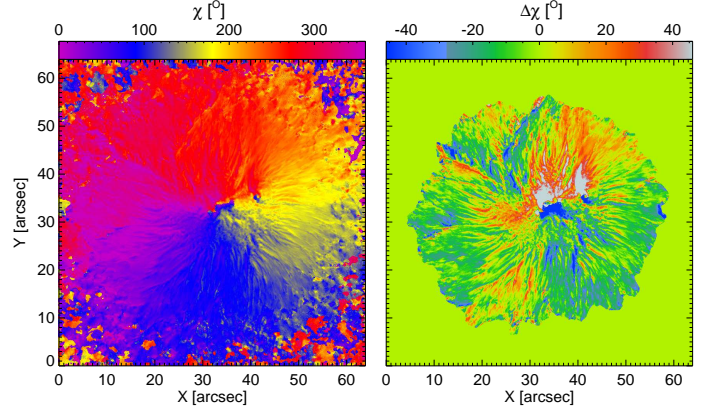


**Fig. 9.** Left panel: field azimuth map at  $\log(\tau) = -0.9$ . Right panel: twist map calculated from the difference between the measured field azimuth and radial directions from sunspot center. To avoid contributions of the azimuth from noisy signal in the quiet surroundings, only pixels lying within the sunspot penumbral boundary are used for computing the twist.

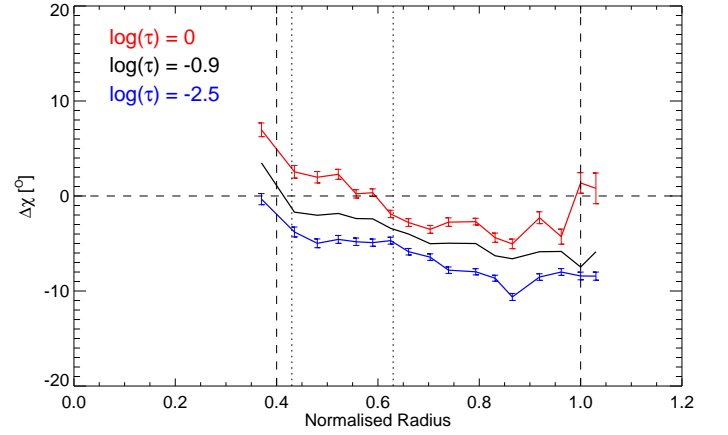


**Fig. 10.** Radial distribution of twist, the azimuthally averaged difference  $\Delta\chi$ , for the sunspot penumbra at three nodes. All vertical lines are the same as in the Fig. 7. The RMS variations are very large along the azimuthal path and not shown here. The error bars represent the standard error of the mean along an azimuthal contour.

To estimate the magnetic twist (average deviation of the field azimuth from the radial direction), we have used only pixels lying within the sunspot boundary. Twist is plotted in the right panel of Fig. 9. We have excluded the quiet-Sun region to avoid the influence of noise and fluctuations. The average twist value of the full sunspot in the bottom layer comes out to be  $-3.8^\circ$ . This value of twist is in agreement with Tiwari et al. (2009), who estimated twist of the same spot a day before by using a potential field as reference instead of the radial field. In agreement with the findings of Tiwari et al. (2009), it is clear from the right panel of Fig. 9 that locally much larger and oppositely directed twists dominate. Sometimes the local twist reaches a value of  $|\Delta\chi| > 90^\circ$ . The estimated azimuthally averaged twist with radius at the three node positions are plotted in Fig. 10. Note, however, that the large twist in the umbra seen in Fig. 9 is partly due to the fact that the geometric and magnetic centers of the spot are not completely co-



located. For this reason only the twist of the penumbral field is plotted in Fig. 10.

In the penumbra, there is a trend of increasing twist with radius as well as with height. In the middle penumbra, average unsigned twist in the lower two nodes is generally less than  $5^\circ$ . Although the variations of the field azimuth along the contours are large, the estimated error in the mean value is not, owing to the large number of pixels along the contours. The error in the mean is indicated in Fig. 10 and is clearly much smaller than the recovered twist values. However, please note that the error bars are not important for the contours having lots of pixels with  $|\Delta\chi| > 90^\circ$ .

It is also worth mentioning here that the field azimuth is the most fluctuating parameter obtained from the inversion. It is also the one most strongly affected by noise. Nonetheless, Fig. 9 does indicate that there could be a gradient in the twist of the sunspot field, both with radial direction and with height.

### 3.4. Mass flux

For a reliable calculation of the mass flux, we require the density and the LOS velocity on a geometrical height scale. Not only can the relative geometric height differences between different points in the field of view not be inferred by the inversion code, the density and vertical height scale is calculated by assuming hydrostatic equilibrium, an assumption that is often not valid in a highly magnetised structure.

Bearing the above limitations in mind and assuming that  $\tau$  unity lies at the same  $z$  at all positions in penumbra, a crude estimate of the mass flux over the full sunspot gives about 2.5 times more downflowing than upflowing mass, in agreement with the estimates of Westendorp Plaza et al. (1997, 2001a) for a sunspot, and with the results of Tiwari et al. (2013) for an averaged sunspot penumbral filament. The amount of excess downflows decreases with height, but even at  $\log(\tau) = -2.5$ , the excess is a factor of about 1.3.

Although a partial contribution to the downflowing mass from the inverse Evershed flow effect through spines cannot be ruled out, this result suggests that the assumptions made when deducing the mass flux e.g., hydrostatic equilibrium,  $\log(\tau) = 0$  located at the same  $z$  for all penumbral pixels, cannot be true. Therefore, a true geometrical height computation is a must to reliably estimate the mass flux over a sunspot.

Finally, the net mass flux depends on the zero level of the velocity. We have set the velocity at the lowest node in the dark parts of the umbra to zero, since the density is highest at that layer. However, if we decide to force the velocity to be zero at the central node ( $\log \tau = -0.9$ ), then the mass flux excess at  $\log(\tau) = 0$  reduces to 1.7 (down from a factor of 2.5).

## 4. Mutual dependence of physical parameters, and sunspot substructures

In this section, we plot two dimensional (2D) histograms of one physical parameter relative to another and investigate their mutual dependences. Then, by isolating different populations in the histograms, we identify specific substructures of the sunspot.

### 4.1. Field strength, $B$ , versus inclination, $\gamma$

2D histograms of  $B$  versus  $\gamma$  of the full sunspot at the three height node positions are shown in the left panels of Fig. 11. A general anticorrelation between  $B$  and  $\gamma$  is found at all depths for  $\gamma \leq 90^\circ$ , in general agreement with Stanchfield et al. (1997); Westendorp Plaza et al. (2001b) and Mathew et al. (2004). A weak positive correlation, not previously reported, is noticeable at all heights in the range  $\gamma = 90^\circ - 180^\circ$  in spite of the relative scarcity of points.

The two peaks in the histograms at all the three heights may be interpreted to belong to the sunspot umbra (the population in the black box shown for  $\log(\tau) = 0$  in Fig. 11e) and the penumbra (the population near  $\gamma = 90^\circ$ ). In an attempt to clarify this picture, we recreated the histograms for penumbral pixels only, shown in the right panels of Fig. 11. From the residual population of the black box, it is clear that the population that we were relating to umbra consists not only of umbra, but to a significant extent also of penumbral pixels. By marking all pixels contained by the black box in Fig. 11(e) in red in Fig. 12(a) and in blue in Fig. 12(b), it becomes clear that some of the pixels in the black box belong to the spines of the penumbra, which appear to be true extensions of the umbra into the penumbra. The two populations of umbral/spine pixels and penumbral filament pixels, which are quite distinct at  $\log(\tau) = 0$ , increasingly merge with height, although the umbral/spine pixels exhibit much less scatter at  $\log(\tau) = -2.5$  than the filament pixels.

The remaining penumbral pixels, including the second population characterized by nearly horizontal fields with an average field strength of 1 kG, consist of penumbral filaments. Penumbral filaments, whose bulk contains a horizontal field with a strength of  $\sim 1$  kG (Tiwari et al. 2013), clearly form the dominant part of the penumbra. The right halves of the frames, with  $\gamma > 90^\circ$ , are populated by the filament tails, where the field is stronger, with a polarity opposite to that of the umbra. The opposite polarity is most prominent at  $\log(\tau) = 0$ , but is also visible in the higher nodes (albeit for fewer pixels), consistent with the field bending back down into the photosphere.

### 4.2. Temperature, $T$ , versus magnetic field strength, $B$

It was first realized by Biermann (1941) that the presence of a strong magnetic field in a sunspot could be responsible for its darkness. Alfvén (1943) predicted a relationship between the magnetic field strength and temperature, which has been extensively investigated theoretically, e.g., by Chitre (1963); Dicke (1970); Cowling (1976); Maltby (1977); Spruit et al. (1990) and observationally, e.g., by Chou (1987); Martínez Pillet & Vázquez (1990); Kopp & Rabin (1992); Martínez Pillet & Vázquez (1993); Westendorp Plaza et al. (2001b); Mathew et al. (2004). However, the relationship between  $B$  and  $T$  of sunspots, particularly the correspondence between different parts of scatter plots found by these authors and features of sunspots, has not been understood yet (see, Solanki 2003, for a detailed review on the subject).

The 2D histograms of  $T$  versus  $B$  in Fig. 13 allows us to revisit the thermal-magnetic relationship of sunspots. The temperature and its spread over different parts of the sunspot decrease rapidly with height. At first glance, the plots for the full sunspot in the left panels appear nearly

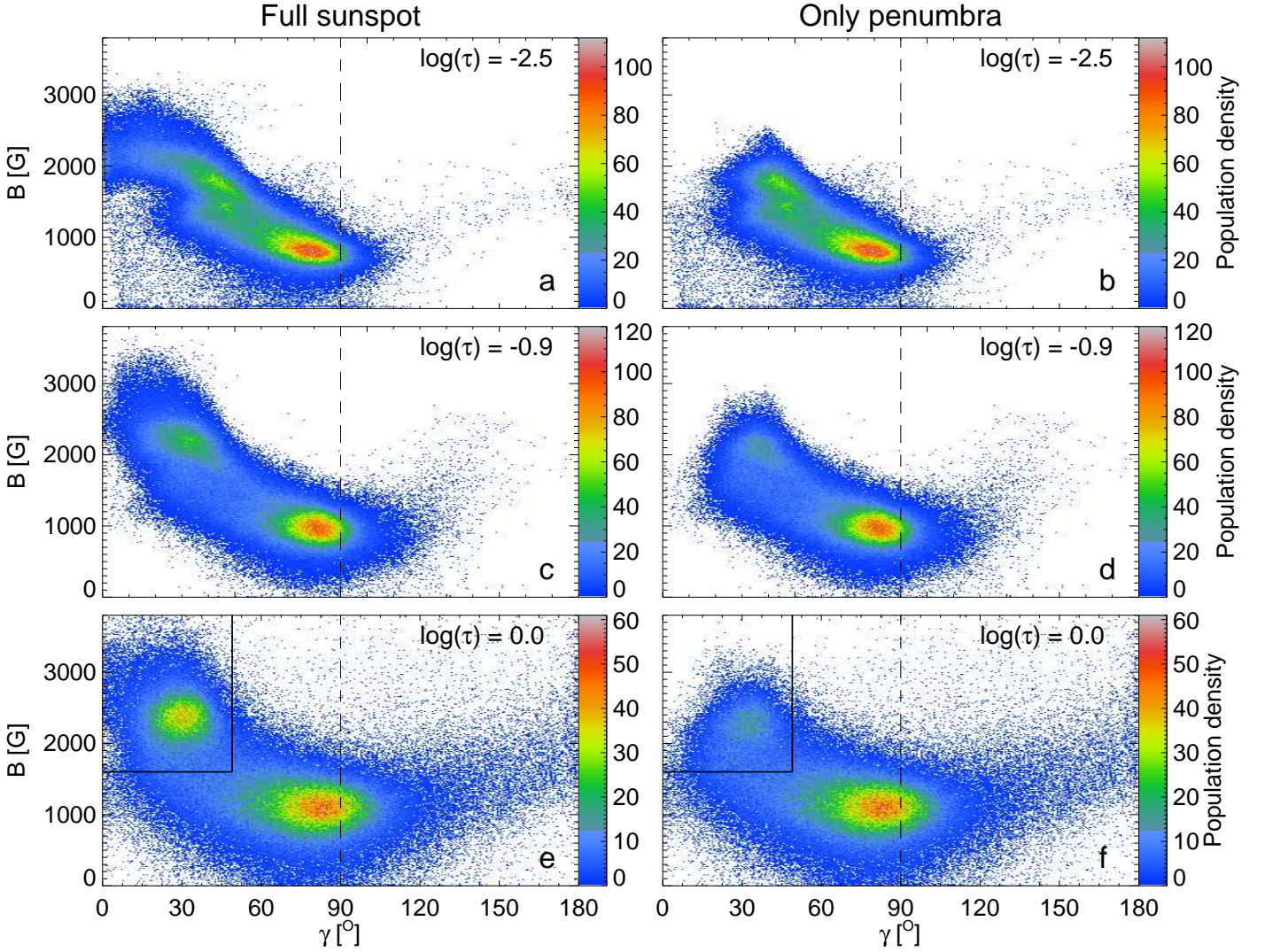


**Fig. 11.** Left panels: 2D scatter plots of  $B$  vs.  $\gamma$  for all points within the sunspot’s boundary at the three optical depth nodes (from top to bottom,  $\log(\tau) = -2.5, -0.9, 0$ ). Right panels: the same but only for pixels in the penumbra. The vertical dashed line in each panel represents the location of  $\gamma = 90^\circ$ . A black box is drawn at  $\log(\tau) = 0$  to identify/outline the umbral pixels, spine pixels in (f) (see Fig. 12(a) and (b) for where these pixels are located in the sunspot).

identical to the results obtained by Kopp & Rabin (1992); Solanki et al. (1993); Martínez Pillet & Vázquez (1993); Stanchfield et al. (1997); Westendorp Plaza et al. (2001b); Penn et al. (2003); Mathew et al. (2004). However, a closer look reveals noticeable differences mainly in the right parts of the plots, which are expected to be populated by penumbral pixels. To confirm this identification, we plotted the same histograms at the three heights for penumbral pixels only, shown in the right panels of Fig. 13. The most densely populated area is at around 1 kG field strength and a temperature of 5900 - 6400 K at  $\log(\tau) = 0$ .

Although the general impression of Fig. 13 is of an anticorrelation (also in the penumbra, where the correlation coefficient is around  $-0.4$ ), we do find a localized weak positive correlation between the two parameters, particularly visible in the region outlined by a black box in Fig. 13(f). The positive correlation between the temperature and the magnetic field strength is probably caused by the brighter heads of the penumbral filaments, which are brighter than their surroundings and often contain a stronger magnetic field (Tiwari et al. 2013). To confirm this, we identified the

locations of the pixels lying in the black box, and highlighted them in Fig. 12(d), which confirms that they are to a significant extent the locations of the heads of penumbral filaments; some pixels, e.g., from the bulk of filaments, appear to be present as well. An additional scatter plot (not shown here) of  $B$  vs.  $T$  for only highlighted pixels confirms this weak positive correlation. It must be noted, however, that not all the heads of penumbral filaments are highlighted by the selection criteria described in Fig. 12(d). For example, some heads may contain a temperature of 6400 K or less, which will then fall outside the box towards lower temperatures and not be highlighted in Fig. 12(d).

Another anomalous, rather scattered, population in the Fig. 13(f) is formed by the pixels above 2500 G and 5500 K (indicated by an arrow). This is formed by the tails of penumbral filaments which have stronger fields and are somewhat darker than the heads of filaments. As shown by Tiwari et al. (2013), the tails of filaments show an enhancement in temperature, thus sometimes becoming hotter than parts of their bulk (see, Fig. 5 of Tiwari et al. 2013). The panels (e) and (f) of Fig. 13, together, show



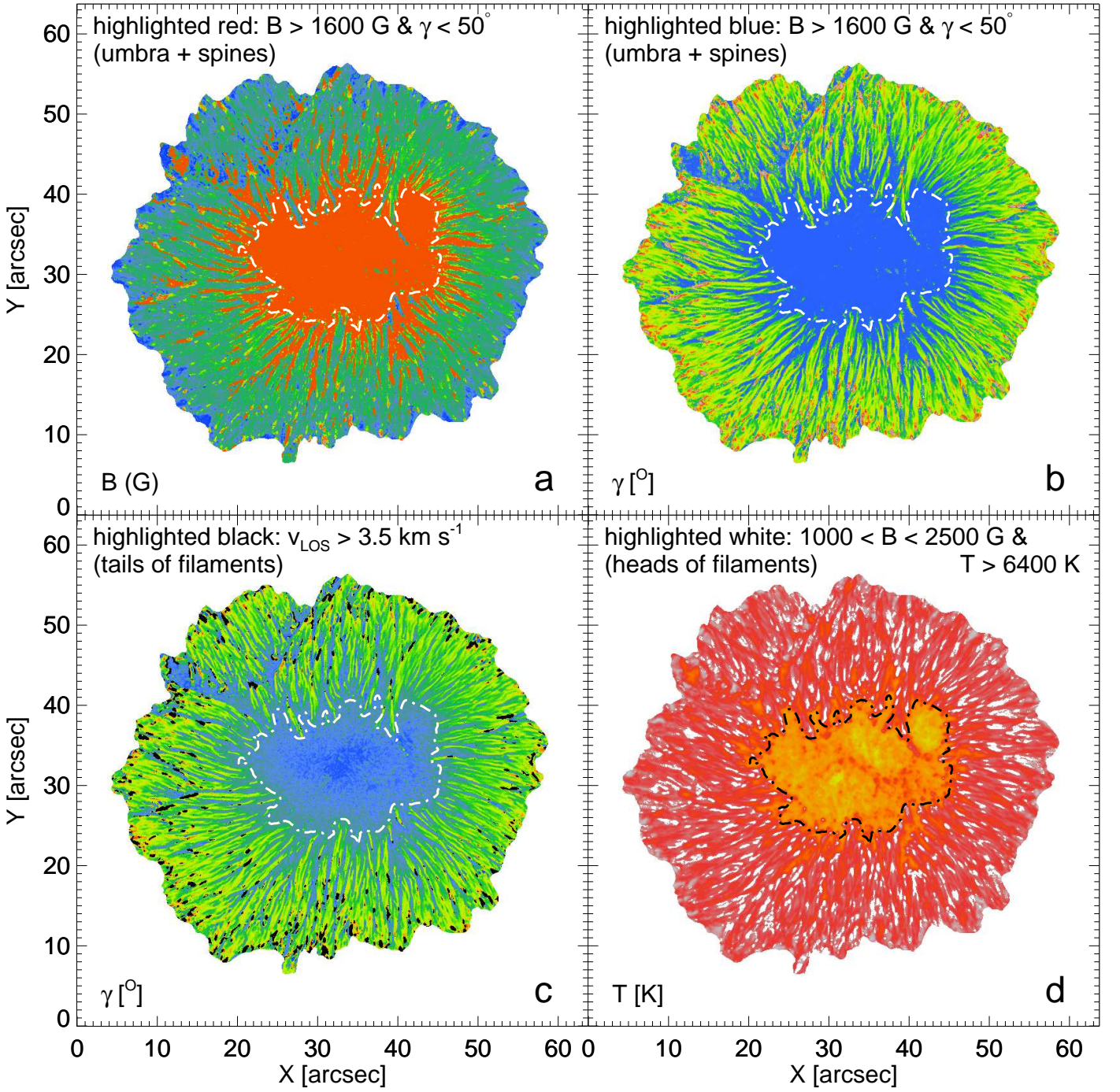


**Fig. 12.** (a): Map of magnetic field strength at  $\log(\tau) = 0$ . The pixels with  $B > 1600$  G &  $\gamma < 50^\circ$  are highlighted in red (i.e., the pixels in the box outlined in black in Figs. 11(e) and 10(f)). (b): Field inclination map at  $\log(\tau) = 0$  with pixels satisfying the same conditions as applied to the field strength map in panel (a) highlighted in blue. The colour scheme for the field inclination map is chosen for consistency with the field inclination map depicted in Fig. 3. (c): Same map as displayed in (b), but pixels with  $v_{\text{LOS}} > 3.5 \text{ km s}^{-1}$  are highlighted in black, revealing tails of penumbral filaments. (d): Map of temperature at  $\log(\tau) = 0$ , highlighted in white are pixels satisfying  $T > 6400$  K &  $1000 < B < 2500$  G, basically representing heads and warm parts of bulks of penumbral filaments. The dash-dotted contour in each panel represents umbra-penumbra boundary.

that the strongest fields in the sunspot either belong to the umbra, or to the tails of penumbral filaments.

els with  $T(> 5500\text{K})$  and  $B(> 2500\text{G})$  of the population indicated by an arrow in Fig. 13(f).

Please note that the highlighted pixels for tails of penumbral filaments in Fig. 12(c), by the condition  $v_{\text{LOS}} > 3.5 \text{ km s}^{-1}$ , as described later, also accommodate the pix-



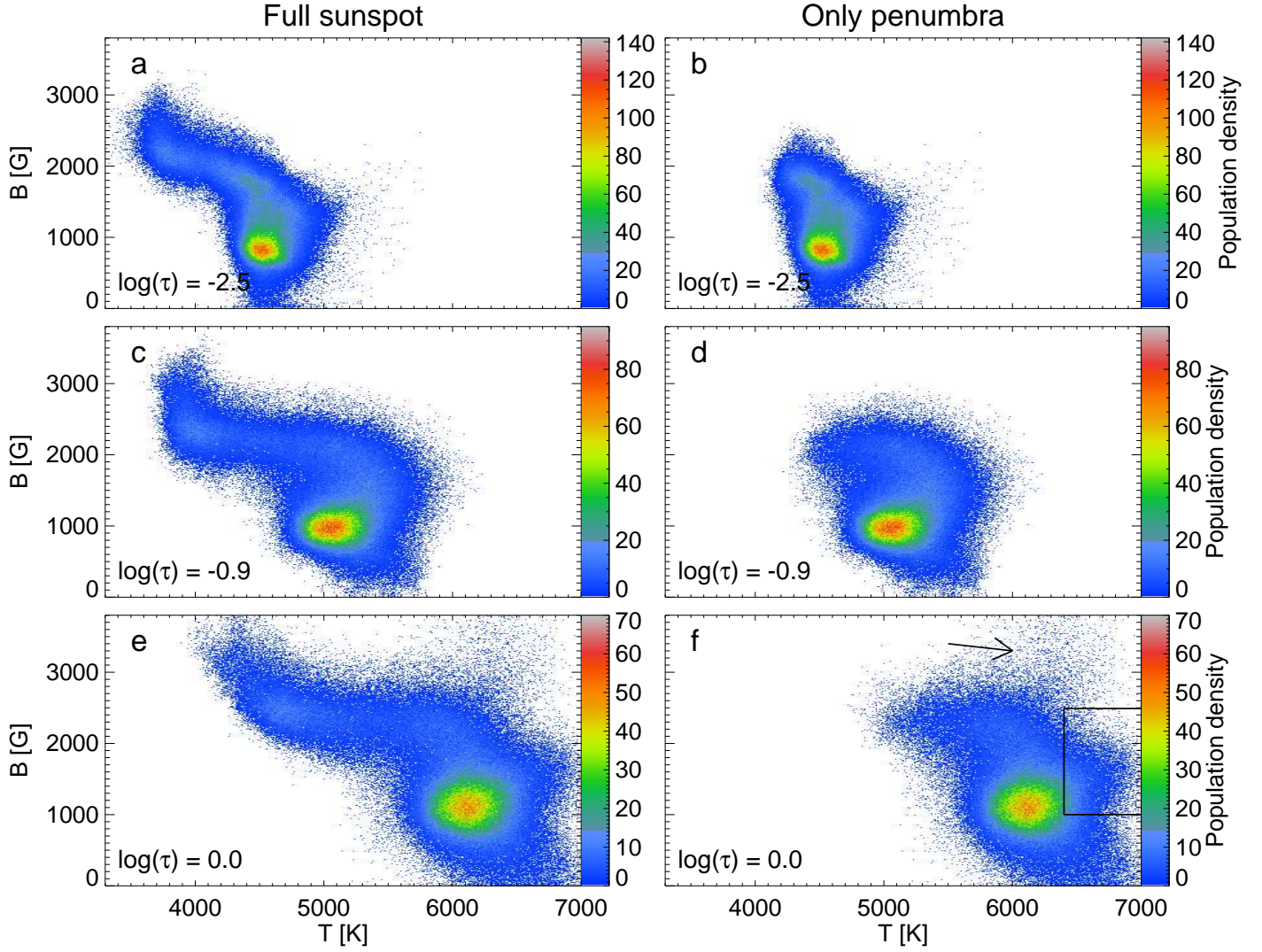


**Fig. 13.** Left panels: 2D scatter plots of  $B$  vs.  $T$  for all pixels. Right panels: The same but only for penumbral pixels inside the sunspot, shown at the optical depths of the three nodes. The black box in (f) outlines the heads of some of penumbral filaments (see, Fig. 12(d) to find the spatial locations of these pixels). The arrow in (f) points to the population that belongs to tails of penumbral filaments, which are subsets of highlighted pixels in Fig. 12(c)).

#### 4.3. LOS velocity, $v_{\text{LOS}}$ , versus temperature, $T$

The upflowing gas is expected to be hotter than the downflowing gas if these flows are driven by convection. 2D histograms of  $v_{\text{LOS}}$  versus  $T$  for the full sunspot at the three node positions are displayed in the left panels of Fig. 14. Most of the coolest pixels (mostly belonging to the umbra) are concentrated around zero velocity, at all the three heights (the horizontal branch of the histograms to the left), with some deviations in the deepest node due to umbral dots (e.g., Riethmüller et al. 2013) and faint light bridges (e.g., Lagg et al. 2014) containing up- and downflows.

The broad distribution of points above roughly 5500 K in all panels is the penumbral contribution, as confirmed by similar histograms of only the penumbral pixels, depicted in the right panels of Fig. 14. Clearly visible is that the upflows at  $\log(\tau) = 0$  are on average hotter than the downflows. The average temperatures of up- and downflows are  $\sim 6300$ , and  $6050$  K, respectively, for full penumbral pixels and  $6600$  and  $6200$  K for the pixels outside the two solid horizontal lines.

There is a weak tendency for the strongest downflows to be warmer than weak downflows.

The hot upflows and cool downflows, particularly the extended populations below and above the horizontal lines, respectively, in the panels (e) and (f) of Fig. 14 can readily be associated with the heads and tails of penumbral filaments. To confirm that the extended population above the upper horizontal line in the Fig. 14(f) belongs to tails of penumbral filaments, we highlighted those pixels in Fig. 12(c). Similarly, we tested that the population below the lower horizontal line in Fig. 14(f) belongs to heads of penumbral filaments, and found that they are accommodated in the highlighted pixels in Fig. 12(d). Please note that the pixels below the lower solid line in Fig. 14(f) are only a small subset of the pixels highlighted in Fig. 12(d).

In Figure 14(f), it can be seen that spines are cooler and contain very low velocities. These spines get cooler with height, and other penumbral pixels merge with them. In the topmost layer, in Figure 14(b), unexplained weak upflows are seen that appear to be cooler than the downflows. Such a phenomenon is well-known in the quiet-Sun, the so-

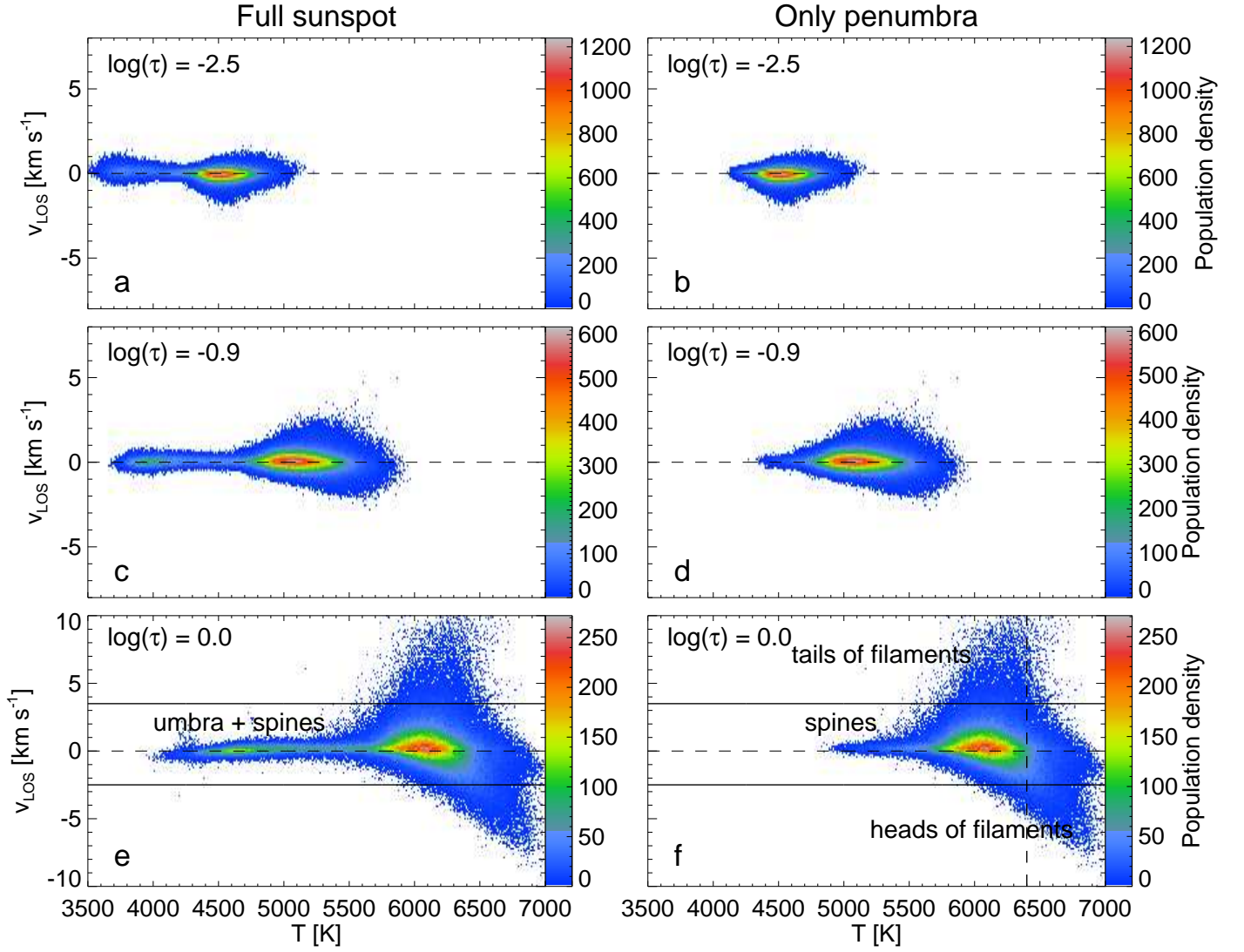


**Fig. 14.** Left panels: 2D scatter plots of  $T$  vs.  $v_{\text{LOS}}$  for all points within the sunspot boundary at the three optical depth nodes. The horizontal dashed line in each panel marks the zero velocity level. In each panel, the points at lower temperature belong to the sunspot umbra and also to spines, those at higher temperature belong only to the penumbra. Right panels: the same, but only for penumbral pixels. The two horizontal solid lines are used to separate, in a rough manner, the heads (lying below the lower solid line) and tails of penumbral filaments (above the upper solid line) from the other points. The dashed vertical line in (f) represents  $T = 6400$  K, a condition applied to isolate the heads of penumbral filaments in Fig. 12(d), although it also includes points from the bulks of the filaments (points to the right of the vertical dashed line lying between the two horizontal solid lines).

called reversed granulation, with granules becoming cooler and intergranular lanes hotter above log optical depth of roughly  $-2$ . We speculate that this (weak) reversal seen at  $\log(\tau) = -2.5$  in the penumbra is the signature of the same effect (described by e.g., Nordlund et al. (2009) to be due to the adiabatic cooling of the expanding upflowing gas).

#### 4.4. LOS velocity, $v_{\text{LOS}}$ , versus magnetic field strength, $B$

In Fig. 15, the 2D histograms of  $v_{\text{LOS}}$  vs.  $B$  are shown, for the whole spot (left panels) and for the penumbra only (right panels). The most prominent features in the histograms are the two branches towards the upper and lower right corners of the domain, most clearly visible at  $\log(\tau) = 0$ . They are readily associated with the tails and heads of penumbral filaments, respectively, and sug-

gest that the strongest magnetic fields are not only found in the umbra, but also in the deepest layers of the fastest downflows, which are expected to lie in the tails of penumbral filaments based on the work of van Noort et al. (2013), and Tiwari et al. (2013).

To confirm the above prediction of the positions of pixels belonging to the heads and tails of penumbral filaments, we have separately overplotted all the pixels outside the two solid horizontal lines shown in Fig. 15(f). As shown in Fig. 12(c), the pixels with  $v_{\text{LOS}} > 3.5 \text{ km s}^{-1}$  nicely match with tails of filaments. The pixels with  $v_{\text{LOS}} < -2.5 \text{ km s}^{-1}$  are found to be completely accommodated within the highlighted pixels of Fig. 12(d).

There is a significant difference of 300 G (1500 G vs. 1800 G) in the field strengths of average up- ( $-3.9 \text{ km s}^{-1}$ ) and downflows ( $5.8 \text{ km s}^{-1}$ ) computed outside the solid lines,

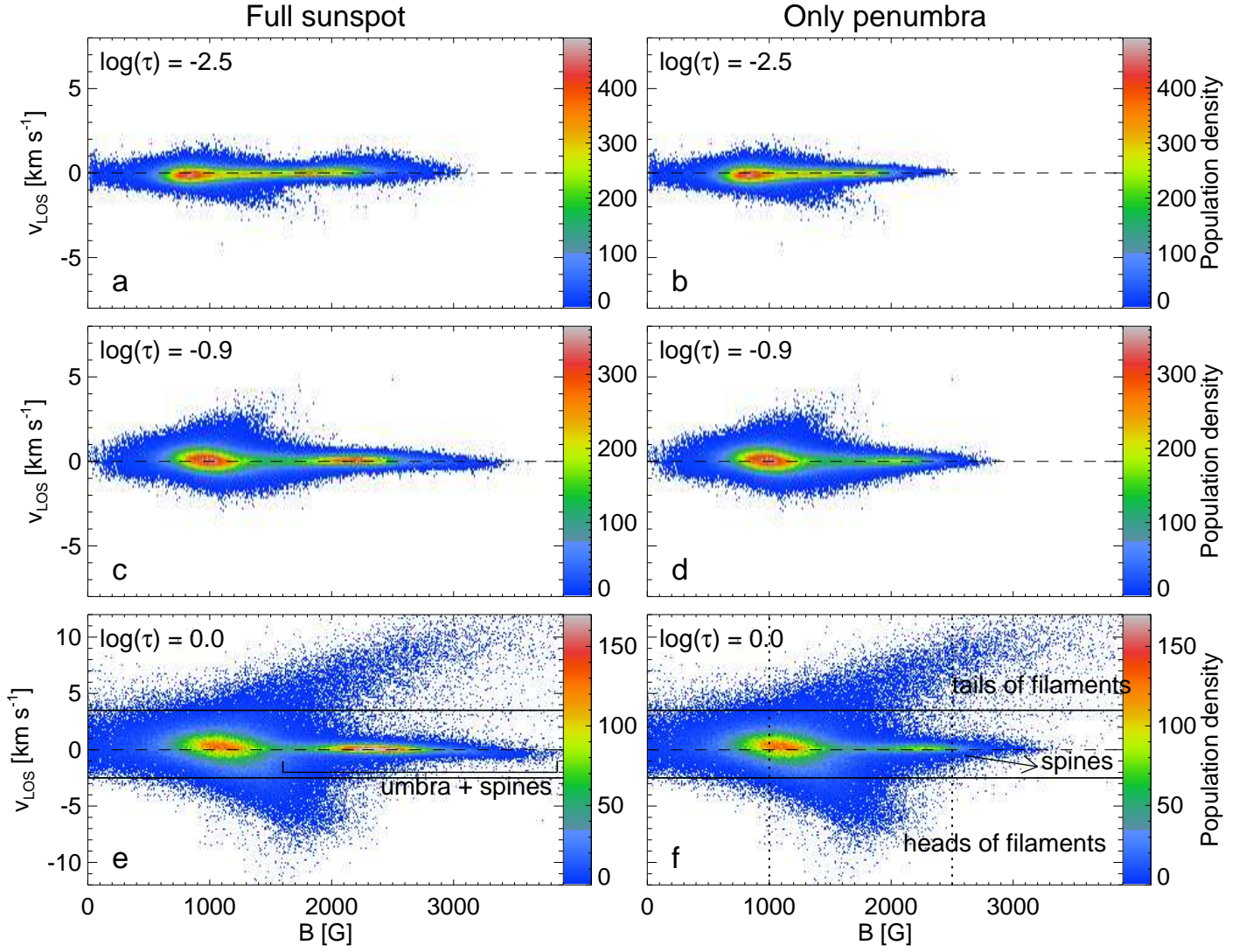


**Fig. 15.** Left panels: 2D scatter plots of  $B$  vs.  $v_{\text{LOS}}$  for all points within the sunspot boundary at the three optical depth nodes. The horizontal dashed line in each panel marks the zero velocity level. Right panels: the same, but only for pixels from the penumbra of the sunspot. The two horizontal solid lines in the panels (e) and (f) indicate thresholds of the velocity used to identify, in a rough manner, the heads and tails of the penumbral filaments. The two vertical dashed lines in panel (f) bound the field strength range  $1000 < B < 2500$  G, a condition used to identify heads of penumbral filaments in Fig. 12(d).

the later being stronger. This difference can generate an outflow via a siphon flow if it refers to the same geometrical height (Meyer & Schmidt 1968; Montesinos & Thomas 1997). However, the higher average temperature (6600 K) of upflows than downflows (that is 6200 K) supports the convection mechanism as the driver of the Evershed flow. Thus, a conclusive statement about the driving mechanism of the Evershed flow cannot be made.

The reduced population of spine pixels in the left and right panels of Fig. 15 at all heights, again shows that the sunspot umbra and spines exhibit similar physical properties. A rapid reduction in both the up- and downflows with increasing height is in agreement with the literature (see e.g., Westendorp Plaza et al. 2001a; Solanki 2003, and references therein). A weak tendency of a shift from overall dominant downflows to weak dominant upflows with increasing height can be seen, however.

## 5. Discussion

We have performed depth-dependent, spatially coupled inversions of a disk-centered sunspot observed by Hinode SOT/SP and have presented the depth-stratified thermal, velocity and magnetic atmospheric structure of it. We have also looked at how the small-scale structures fit in with the global behavior of the sunspot and have introduced simple thresholds in individual parameters to isolate some of the fundamental constituents of the sunspot penumbrae. In the following, we interpret our results and discuss them in the context of earlier work available in the literature.

### 5.1. Global properties

The continuum intensity and temperature at  $\log(\tau) = 0$  display a very similar trend, an obvious increase with radius starting from the center of the spot. The horizontal gradient gets smoother for higher lay-



ers. Results imply that the vertical temperature gradient in the sunspot penumbra is slightly smaller than that in the quiet Sun, but is much larger than that in the umbra. These results are in good agreement with findings in the literature (see, e.g., Schröter 1971; Maltby et al. 1986; Collados et al. 1987; Lites et al. 1993; Stanchfield et al. 1997; Westendorp Plaza et al. 2001b; Solanki 2003; Tritschler et al. 2004).

The azimuthally averaged magnetic field strength decreases with radial distance from the center of the sunspot (2800 G) to the outer penumbral boundary (700 G at  $\tau$  unity level), in qualitative agreement with earlier findings, e.g., Westendorp Plaza et al. (2001b); Mathew et al. (2003); Borrero & Ichimoto (2011). However, some quantitative differences, beyond the well-known difference in the maximum  $B$  of spots (e.g., Schad 2013) that is known to depend on the size of spots, can be seen. E.g., the averaged field strength values of about 2300 G, and 2500 G for umbra, and 500 G, and 700 G for outer penumbral boundaries, found by Westendorp Plaza et al. (2001b), and Mathew et al. (2003), respectively, might be due to the variation of properties from one sunspot to another; see also Solanki (2003), but may also reflect differences in the spectral lines used and the spatial resolution of the data. The maximum  $B$  in our sunspot is comparable to that of the sunspots with similar areas in the work of Schad (2013).

The vertical gradient in the photospheric layers of the umbra of  $-1.4 \text{ G km}^{-1}$  is comparable to that obtained in the most recent MHD simulations (e.g.,  $-1.5 \text{ G km}^{-1}$ : M. Rempel, 2013, private communication). In the literature, vertical field gradient values in sunspot umbrae varying from  $-4 \text{ G km}^{-1}$  (Westendorp Plaza et al. 1998) to  $-1.5 \text{ G km}^{-1}$  (Collados et al. 1994; Westendorp Plaza et al. 2001b; Balthasar & Gömöry 2008) have been reported, but see also Schröter (1971) for smaller vertical field gradients of about  $-0.5 \text{ G km}^{-1}$ . For a detailed review of earlier results, see Solanki (2003).

The positive vertical magnetic field gradient observed in the middle part of the sunspot penumbra is partly caused by the partial cancellation of the Stokes  $V$ —signal at the unresolved interface between the spines and the partly oppositely directed field at the edges of the filaments near their heads but is also an artifact of the highly corrugated iso- $\tau$  surface in the inner penumbra, see Balthasar & Gömöry (2008); Balthasar et al. (2013); Joshi (2014); Joshi et al. (2015). The last two investigations present a particularly thorough analysis of such observations.

The main indication of a magnetic canopy in our inversion results is the presence of stronger field at the upper node than at the two lower nodes. Such a signature is found only outside the sunspot. This agrees with earlier findings of Giovanelli (1980); Giovanelli & Jones (1982); Solanki et al. (1992, 1994, 1999); Adams et al. (1993); Balthasar & Gömöry (2008), but partly differs from the results of Westendorp Plaza et al. (2001b), who found a canopy-like structure starting from the middle of the penumbra and continuing outside the penumbral boundary of their spot. A similar canopy-like structure to that found by Westendorp Plaza et al. (2001b) was reported more recently by Borrero & Ichimoto (2011). The fact that Mathew et al. (2003) found no canopy structure even outside the visible boundary of their sunspot, is likely due to the much lower formation height of the  $1.56 \mu\text{m}$  lines they used and thus need not be inconsistent with our results.

Note that the sunspot canopies inferred from the  $1.56 \mu\text{m}$  lines by Solanki et al. (1992, 1994) were deduced using another technique and not from the explicit height-dependent inversion of spectral lines. Although not so clearly marked, a canopy structure outside the sunspot boundary, similar to that obtained here, was seen by Balthasar & Gömöry (2008).

The larger azimuthally averaged inclination of the field (i.e., on average more horizontal field) in the lower layers throughout the spot, by about  $10^\circ$ , is consistent with the findings of Westendorp Plaza et al. (2001b) and Borrero & Ichimoto (2011), who attributed this to the field canopy structure starting in the inner penumbra. However, it disagrees with the finding by Mathew et al. (2003) that the field becomes more horizontal with height. This disagreement could be caused by the different formation height of the IR lines used by Mathew et al. (2003), or by the larger influence of straylight on their results.

Although in a simple monolithic flux-tube model of a sunspot we expect the field to be more vertical with height, a change of  $10^\circ$  within the lower photosphere is too large to be explained in the context of a homogeneous flux-tube model. Instead, it can be understood in terms of small-scale structure. Umbral dots and light bridges, containing more strongly horizontal fields than the umbral background, are visible only in the deepest layers (see e.g., Riethmüller et al. 2013; Lagg et al. 2014, for umbral dots and light bridges, respectively, and references therein), but do not contribute to the averaged inclination at higher layers. Similarly, in the penumbra, the restriction of the mainly horizontal-field penumbral filaments to the low photosphere and the wrapping of the magnetic field around them (Borrero et al. 2008; Tiwari et al. 2013) leaves only a relatively vertical field in the upper layers of the solar photosphere, as proposed by Solanki & Montavon (1993).

The general inverse relationship between the magnetic field strength,  $B$ , and its inclination  $\gamma$ , is well known from earlier observations with lower spatial resolution (Solanki et al. 1993; Stanchfield et al. 1997; Westendorp Plaza et al. 2001b; Mathew et al. 2004). We revisit this relationship with our high resolution data set and find a stronger anti-correlation between these two parameters than obtained by earlier researchers, e.g., Westendorp Plaza et al. (2001b). We also find the presence of two populations, clearly separated at  $\log(\tau) = 0$ , one of umbral and of penumbral spine pixels, the other of penumbral filament pixels. At higher layers the two populations merge, possibly because the spines expand and their field wraps around the filaments.

Another novel feature that we find is a positive correlation between the field strength and the inclination for  $\gamma > 90^\circ$ , most eminently at  $\log(\tau) = 0$ . We attribute it to the tails of the penumbral filaments, which contain opposite polarity, stronger magnetic field (Tiwari et al. 2013).

It has been known for decades that the darker umbral regions contain more intense magnetic fields (Kopp & Rabin 1992; Martínez Pillet & Vázquez 1993; Stanchfield et al. 1997; Westendorp Plaza et al. 2001b; Solanki 2003). We confirm the general relationship at all heights. In qualitative agreement with the earlier researchers, we find that the darker and therefore cooler regions contain stronger fields in the umbra at all heights with a dependence roughly in the shape of a raised elephant's trunk (see Fig. 13), particularly visible in the upper two

node positions, indicating that the temperature is nearly constant for a range of the strongest umbral fields.

In the penumbra, however, this relation is not universally valid. The heads of penumbral filaments contain strong fields (Tiwari et al. 2013), yet they are bright, giving rise to a positive correlation between the temperature and magnetic field in the sunspot penumbra. In the early literature, this positive correlation between temperature and field was mis-interpreted as an indication that the spines are the brighter parts of the sunspot penumbra e.g. Westendorp Plaza et al. (2001b), see a review by Solanki (2003), and Tiwari et al. (2013) for detailed clarification.

The average LOS velocity shows dominant upflows (peak at  $\sim -300 \text{ ms}^{-1}$ ) in the inner penumbra and downflows (peak at  $\sim 1300 \text{ ms}^{-1}$ ) in the outer penumbra, in qualitative agreement with earlier observations (e.g. Rimmele 1995b; Schlichenmaier & Schmidt 2000; Westendorp Plaza et al. 2001a; Tritschler et al. 2004; Sánchez Almeida et al. 2007; Ichimoto et al. 2007a; Franz & Schlichenmaier 2009). This observation supports the scenario of the Evershed flow rising in the inner penumbra and sinking in the outer penumbra. This average flow pattern is the sum of the flows in individual penumbral filaments. The upflows are concentrated in the heads, the downflows in the tails of individual filaments (Tiwari et al. 2013). Since the heads are closer to the umbra, the tails closer to the outer boundary of the spot, azimuthal averaging produces upflows in the inner and downflows in the outer penumbra. The upflows along the axis of the filaments and downflows along their sides (Tiwari et al. 2013) partly average out during the azimuthal averaging and contribute less to the global radial trend.

An average downflow of about  $350 \text{ ms}^{-1}$  is seen over the sunspot penumbra at  $\log(\tau) = 0$ , caused by the presence of strong downflows at the outer penumbral boundary. The strong downflows are found to continue outside the outer penumbral boundary, even reaching a maximum there in the azimuthal averages (see, Fig. 6). This is in agreement with the results of, e.g., Sheeley (1972); Dere et al. (1990); Böerner & Kneer (1992); Solanki et al. (1994) that a part of the mass transported by the Evershed flow continues beyond the sunspot's visible boundary.

We can see in Fig. 6 that the azimuthally averaged velocity in the two top nodes is not zero in the umbra, but instead shows an average downflow that increases with height. Since the density decreases rapidly with height, any downward mass flow would result in such a height dependence of the velocity. This downflow could be a result of the inverse Evershed flow (Maltby 1975).

The clear pattern of hotter upflows than downflows in the sunspot penumbra (by an average difference of about 400 K between heads and tails of penumbral filaments) is consistent with the transport of heat by convective motions in the sunspot penumbra, as has variously been proposed to explain the observed penumbral brightness (Danielson 1961; Chitre 1963; Meyer et al. 1974; Weiss 1991; Jahn & Schmidt 1994; Schüssler & Knölker 2001; Weiss 2002; Weiss et al. 2004; Thomas & Weiss 2008; Rempel et al. 2009b). At the same time, however, the downflow speed is correlated with field strength, and strong downflows are associated with stronger fields than upflows (by an average difference of about 300 G between heads and tails of filaments). This result is consistent with the requirements of the siphon flow model

(Meyer & Schmidt 1968; Montesinos & Thomas 1997). Therefore, the up- and downflows in the penumbra exhibit properties that make them partly consistent with both the main rivaling theories of the Evershed flow (the flux tube: Solanki & Montavon (1993); Schlichenmaier et al. (1998a,b); Borrero et al. (2005), and field free gap models: Spruit & Scharmer (2006); Scharmer & Spruit (2006)). One caveat is that to test the siphon flow we need to know  $v$  and  $B$  at a given geometrical height, which is not fulfilled (to an unknown extent) by the present data.

The average azimuthal twist within the sunspot penumbra for the deepest layers was found to be  $-3.8^\circ$ , which is in agreement with the twist found by Tiwari et al. (2009) for this spot as observed one day earlier, estimated by computing the spatially averaged signed shear angle, which returns the twist of a spot irrespective of its shape and force-free nature of the field. The twist in the spot increases with the radius as well as with height. The increase in the twist with height can be understood as a result of the expansion of a twisted flux tube which leads to an increase in the azimuthal component of magnetic field, in turn resulting in an increase in the measured twist (from  $\tan^{-1}(B_\psi/B_r)$  according to Venkatakrisnan & Tiwari (2009)) (see, e.g., Parker 1974, 1975, 1979). The increase in the twist with radius might be a result of the Coriolis force acting on the outflowing material of the Evershed flow. This effect becomes stronger at larger radii in the penumbra due to the weaker average field (see, e.g., Peter 1996). A caveat on the determined twist worth mentioning is given by the results of Bühler (2013), who found systematic unexplained positive twist in all features of both the magnetic polarities.

A crude estimate of the mass flux over the full sunspot suggests that the downflowing mass is about 2.5 times larger than the upflowing mass. This result is in agreement with that obtained by Westendorp Plaza et al. (1997) for a full sunspot and by Tiwari et al. (2013) for a standard penumbral filament. The latter authors suggested that this excess downflow can be attributed to the corrugation of the surfaces of constant optical depth within penumbral filaments. In contrast, Puschmann et al. (2010) found the upflowing mass flux to be five times larger than the downflowing mass flux in part of a sunspot penumbra. As described in Tiwari et al. (2013), this inconsistency could be because of Puschmann et al. (2010) evaluating mass flux on the inner part of penumbra where upflows dominate due to the dominant presence of heads of penumbral filaments and also partially because they took the diskward part of the penumbra, which is blueshifted due to the Evershed flow. Another factor that could contribute to the difference is that Puschmann et al. (2010) estimated the mass flux on a surface of constant geometrical height which they deduced based on the requirement of  $\text{div}\mathbf{B} = 0$ , whereas ours and that of Westendorp Plaza et al. (1997) was calculated on a surface of constant optical depth.

## 5.2. Constituents of the penumbra

The filamentary nature of the sunspot penumbra has been investigated for more than 50 years, e.g., Danielson (1964); Moore (1981b,a); Title et al. (1993); Lites et al. (1993); Rimmele (1995a); Langhans et al. (2005); Ichimoto et al. (2007b); Borrero et al. (2008); Borrero & Ichimoto (2011); Joshi et al. (2011); Scharmer et al. (2011); Scharmer & Henriques (2012); Scharmer et al. (2013);

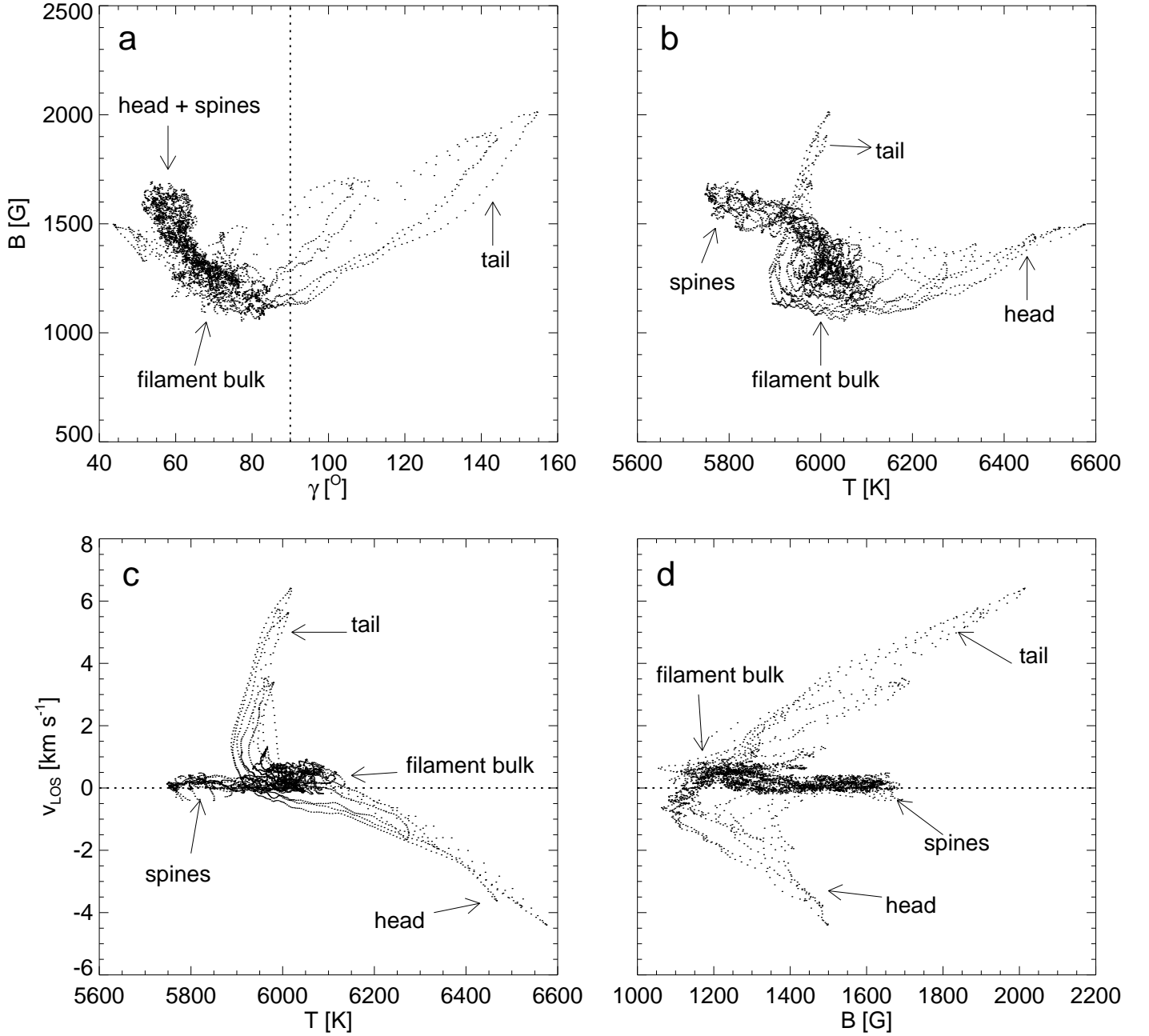


**Fig. 16.** Scatter plots of different physical parameters of the standard penumbral filament studied by Tiwari et al. (2013). The selected area also contains pixels belonging to the surroundings of the filament (spines). All plots are for the height  $\log(\tau) = 0$ . The four panels show scatter plots between (a) the field strength  $B$  and inclination  $\gamma$ , (b)  $B$  and temperature  $T$ , (c) the line-of-sight velocity  $v_{\text{LOS}}$  and  $T$ , (d)  $v_{\text{LOS}}$  and  $B$ . The vertical line in (a.) marks  $\gamma = 90^\circ$ ; horizontal lines in panels (c) and (d) represent  $v_{\text{LOS}} = 0$ . Different parts of the filaments are identified in each plot.

Tiwari et al. (2013). One proposal to divide the sunspot penumbra into two components, spines: the more vertical and stronger fields, and interspines: more horizontal and weaker fields, was given by Lites et al. (1993). Our results clearly show (see, Fig. 12) that the spines have properties similar to the umbra, but with increasing field inclination and decreasing field strength radially outwards. It is worth mentioning that these locations (umbra and spines) are found to more closely satisfy force-free conditions on the photosphere than other parts of sunspots (Tiwari 2012).

The remainder of the penumbra resembles the standard penumbral filament presented by Tiwari et al. (2013), who

showed that the penumbral filaments display similar properties as stretched granules. They found that penumbral filaments contain strong upflows at their heads and downflows at their tails. The upflows continue along the central axis of filaments to more than half of their lengths, surrounded by weak downflows on both the sides of filaments, signatures of which were already reported by e.g., Joshi et al. (2011); Scharmer et al. (2011), and Scharmer & Henriques (2012). The locations of these lateral downflows near heads of filaments were found to contain opposite polarity field to that of umbra, spines and heads of filaments in one third of the penumbral filaments that Tiwari et al. (2013)



studied, in agreement with the results of Rempel (2012); Ruiz Cobo & Asensio Ramos (2013) and Scharmer et al. (2013). Additional features, often counted as constituents of the penumbra, such as penumbral grains, turned out to be heads of penumbral filaments.

In Fig. 16 we display scatter plots of a number of physical quantities at  $\log(\tau) = 0$  from the standard penumbral filament created by Tiwari et al. (2013). Note that by choosing a fixed width for all filaments contributing to the standard filament, the latter also includes parts of neighbouring spines at its sides and around at its head. The contributions of different parts of the filament to the clouds of data points are marked by arrows.

A comparison of the scatter plots in Fig. 16(a), (b), (c), (d) with Figs 11(f), 13(f), 14(f), and 15(f), respectively, reveals strong similarities, supporting our speculation that penumbrae can be described as a combination of spines and filaments. The main difference is the lower scatter in Fig. 16 due to the averaging done to produce the standard filament. The smoothness (e.g., of spines) and the fact that many points describe curves in scatter plots of the standard filament is a result of averaging and bicubic spline interpolation along the length of filaments (for details, see, Tiwari et al. 2013). In addition, the surroundings of filaments in the outer penumbra contain fewer spines. Instead filaments lie directly next to each other, thus diluting the values for spines and making them smoother in the scatter plots.

## 6. Conclusions

Using the SPINOR inversion code, we performed a spatially coupled, depth-dependent inversion of a sunspot observed almost at solar disk center by the Hinode (SOT/SP). We investigated the spot's thermal, velocity and magnetic structure. The average vertical field gradient in the sunspot umbra near the deepest node is  $-1.4 \text{ G km}^{-1}$ , which is in agreement with that found in the recent MHD simulations. The azimuthally averaged magnetic field and inclination show a global general trend as known from earlier work, i.e., the field strength decreases with the radial distance from spot center and with height, the field inclination increases with radius, but decreases with height. A positive vertical gradient of the magnetic field strength in the middle of the penumbra is found that could be the result of either a strongly corrugated optical depth surface in the penumbra, or signal cancellation of unresolved fine structure in the deep photosphere, or a combination of both (see, Joshi et al. 2015). We also find a magnetic canopy structure outside the visible boundary of the penumbra. The temperature displays a slightly stronger vertical gradient in the quiet Sun than in the penumbra, but much stronger than in the umbra. The flatter  $T(\tau)$  profile of the umbra is in agreement with earlier investigations (see, e.g., Solanki 2003, and references therein).

The strongest fields are found in the darkest regions of the umbra, but also in the nearly vertical, opposite polarity flux concentrations in the tails of penumbral filaments. Horizontal fields in the penumbra show an average field strength of 1 kG, in agreement with that obtained in the bulk of a standard penumbral filament by Tiwari et al. (2013).

The well-known general trend of the magnetic field being strongest in the darkest regions is found in the umbra

and in spines. However, in penumbral filaments, in particular at their heads and in their tails, the opposite trend is found. The field azimuth shows an average negative twist of  $< 5^\circ$ . The twist in the penumbra increases both with radial distance from spot center and with height.

Azimuthally averaged line-of-sight velocities at the deepest layer display an upflow (of  $300 \text{ m s}^{-1}$ ) in the inner penumbra, where the number of filament heads harboring strong upflows is largest. In the outer penumbra, where the tails of filaments outnumber the heads, an average downflow of  $1300 \text{ m s}^{-1}$  is observed. On average, the sunspot penumbra contains a downflow of  $\sim 350 \text{ m s}^{-1}$ . All over the sunspot penumbra upflows are found to be hotter (by about 400 K) than downflows, thus, qualitatively supporting the thesis that convection accounts for the observed brightness of the penumbra and is responsible for driving the Evershed flow. However, we also find that strong downflows are on average associated with stronger fields (by about 300 G) than upflows, as required by the siphon flow model. Therefore, these data do not in themselves allow distinguishing between these two mechanisms, partly because the actual geometric height corresponding to a given  $\tau$  level is unknown.

A crude estimate of the mass flux over the full sunspot reveals that the total downflow of mass exceeds the total upflowing mass by a factor of  $\sim 2.5$ . This imbalance is probably a consequence of the optical depth corrugation. Since the upflows are associated with hotter and less strongly magnetized gas than the downflows, we expect that the upflows are detected at a larger height than the downflows. Thus any upflowing mass that turns over and flows down again between these two levels is not detected, although the associated downflow is seen, giving rise to an excess in the downflowing mass.

We find that the spines in the penumbra display qualitatively similar characteristics as the umbra. They are, however, warmer and have a weaker and more inclined field, consistent with their larger distance from the center of the spot.

The scatter plots of the different physical quantities of the standard filament including its surroundings, show a qualitative similarity with the scatter plots of the same quantities for the full penumbra. In particular, the standard filament shows all the populations of points that are also visible in scatter plots of the whole penumbra. This confirms that the spines together with the penumbral filaments are the fundamental constituents of the sunspot penumbra. In particular, this similarity suggests that there are no further major components of the penumbra besides these two.

*Acknowledgements.* We would like to thank the referee for constructive comments. SKT would like to thank Ron Moore, Allen Gary, David Hathaway, and Mitzi Adams for their useful comments and/or discussion on this work. Hinode is a Japanese mission developed and launched by ISAS/JAXA, collaborating with NAOJ as a domestic partner, NASA and STFC (UK) as international partners. Scientific operation of the Hinode mission is conducted by the Hinode science team organized at ISAS/JAXA. This team mainly consists of scientists from institutes in the partner countries. Support for the post-launch operation is provided by JAXA and NAOJ (Japan), STFC (U.K.), NASA (U.S.A.), ESA, and NSC (Norway). This work has been partially supported by the BK21 plus program through the National Research Foundation (NRF) funded by the Ministry of Education of Korea. SKT is supported by an appointment to the NASA Postdoctoral Program at the NASA Marshall Space Flight Center, administered by Oak Ridge Associated Universities through a contract with NASA. This research has made extensive use of NASA's Astrophysics Data System (ADS).

# References

- Adams, M., Solanki, S. K., Hagyard, M., & Moore, R. L. 1993, *Sol. Phys.*, 148, 201
- Albregtsen, F., Joras, P. B., & Maltby, P. 1984, *Sol. Phys.*, 90, 17
- Albregtsen, F. & Maltby, P. 1978, *Nature*, 274, 41
- Albregtsen, F. & Maltby, P. 1981, *Sol. Phys.*, 71, 269
- Alfvén, H. 1943, *Arkiv for Astronomi*, 29, 1
- Balthasar, H., Beck, C., Gömöry, P., et al. 2013, *Central European Astrophysical Bulletin*, 37, 435
- Balthasar, H. & Gömöry, P. 2008, *A&A*, 488, 1085
- Barklem, P. S., O'Mara, B. J., & Ross, J. E. 1998, *MNRAS*, 296, 1057
- Bellot Rubio, L. R., Balthasar, H., & Collados, M. 2004, *A&A*, 427, 319
- Biermann, L. 1941, *Vierteljahresschrift der Astronomischen Gesellschaft*, 76, 194
- Böerner, P. & Kneer, F. 1992, *A&A*, 259, 307
- Borrero, J. M. & Ichimoto, K. 2011, *Living Reviews In Solar Physics*, 8, 4
- Borrero, J. M., Lagg, A., Solanki, S. K., & Collados, M. 2005, *A&A*, 436, 333
- Borrero, J. M., Lites, B. W., & Solanki, S. K. 2008, *A&A*, 481, L13
- Bühler, D. 2013, PhD thesis, Göttingen University, Analysis of small scale magnetic fields using Hinode SOT/SP
- Chitre, S. M. 1963, *MNRAS*, 126, 431
- Chou, D.-Y. 1987, *ApJ*, 312, 955
- Collados, M., del Toro Iniesta, J. C., & Vazquez, M. 1987, *Sol. Phys.*, 112, 281
- Collados, M., Martínez Pillet, V., Ruiz Cobo, B., del Toro Iniesta, J. C., & Vázquez, M. 1994, *A&A*, 291, 622
- Cowling, T. G. 1976, *MNRAS*, 177, 409
- Danielson, R. E. 1961, *ApJ*, 134, 289
- Danielson, R. E. 1964, *ApJ*, 139, 45
- Dere, K. P., Schmieder, B., & Alissandrakis, C. E. 1990, *A&A*, 233, 207
- Dicke, R. H. 1970, *ApJ*, 159, 25
- Evershed, J. 1909, *MNRAS*, 69, 454
- Franz, M. 2011, *ArXiv e-prints*
- Franz, M. & Schlichenmaier, R. 2009, *A&A*, 508, 1453
- Frutiger, C. 2000, Diss. ETH, Inversions of Zeeman Split Stokes Profiles: Application to solar and stellar surface structures, Vol. 13896
- Frutiger, C., Solanki, S. K., Fligge, M., & Bruls, J. H. M. J. 2000, *A&A*, 358, 1109
- Giovanelli, R. G. 1980, *Sol. Phys.*, 68, 49
- Giovanelli, R. G. & Jones, H. P. 1982, *Sol. Phys.*, 79, 267
- Ichimoto, K., Lites, B., Elmore, D., et al. 2008, *Sol. Phys.*, 249, 233
- Ichimoto, K., Shine, R. A., Lites, B., et al. 2007a, *PASJ*, 59, 593
- Ichimoto, K., Suematsu, Y., Tsuneta, S., et al. 2007b, *Science*, 318, 1597
- Jahn, K. & Schmidt, H. U. 1994, *A&A*, 290, 295
- Joshi, J. 2014, PhD thesis, Technischen Universität, Braunschweig, Magnetic and Velocity Field of Sunspots in Photosphere and Upper Chromosphere
- Joshi, J., Lagg, A., Hirzberger, J., Solanki, S. K., & Tiwari, S. K. 2015, *A&A*, 00, to be submitted
- Joshi, J., Pietarila, A., Hirzberger, J., et al. 2011, *ApJ*, 734, L18
- Katsukawa, Y. & Jurčák, J. 2010, *A&A*, 524, A20
- Kopp, G. & Rabin, D. 1992, *Sol. Phys.*, 141, 253
- Kosugi, T., Matsuzaki, K., Sakao, T., et al. 2007, *Sol. Phys.*, 243, 3
- Kubo, M., Lites, B. W., Ichimoto, K., et al. 2008, *ApJ*, 681, 1677
- Lagg, A., Solanki, S. K., van Noort, M., & Danilovic, S. 2014, *A&A*, 568, A60
- Landi Degl'Innocenti, E. & Landi Degl'Innocenti, M. 1977, *A&A*, 56, 111
- Langhans, K., Scharmer, G. B., Kiselman, D., Löfdahl, M. G., & Berger, T. E. 2005, *A&A*, 436, 1087
- Leka, K. D., Barnes, G., Crouch, A. D., et al. 2009, *Sol. Phys.*, 260, 83
- Lites, B. W., Elmore, D. F., Seagraves, P., & Skumanich, A. P. 1993, *ApJ*, 418, 928
- Lites, B. W. & Ichimoto, K. 2013, *Sol. Phys.*, 283, 601
- Maltby, P. 1975, *Sol. Phys.*, 43, 91
- Maltby, P. 1977, *Sol. Phys.*, 55, 335
- Maltby, P., Avrett, E. H., Carlsson, M., et al. 1986, *ApJ*, 306, 284
- Martínez Pillet, V. & Vázquez, M. 1990, *Ap&SS*, 170, 75
- Martínez Pillet, V. & Vázquez, M. 1993, *A&A*, 270, 494
- Mathew, S. K., Lagg, A., Solanki, S. K., et al. 2003, *A&A*, 410, 695
- Mathew, S. K., Martínez Pillet, V., Solanki, S. K., & Krivova, N. A. 2007, *A&A*, 465, 291
- Mathew, S. K., Solanki, S. K., Lagg, A., et al. 2004, *A&A*, 422, 693
- Metcalf, T. R. 1994, *Sol. Phys.*, 155, 235
- Meyer, F. & Schmidt, H. U. 1968, *Mitteilungen der Astronomischen Gesellschaft Hamburg*, 25, 194
- Meyer, F., Schmidt, H. U., Wilson, P. R., & Weiss, N. O. 1974, *MNRAS*, 169, 35
- Montesinos, B. & Thomas, J. H. 1997, *Nature*, 390, 485
- Moore, R. L. 1981a, *Space Sci. Rev.*, 28, 387
- Moore, R. L. 1981b, *ApJ*, 249, 390
- Nordlund, Å., Stein, R. F., & Asplund, M. 2009, *Living Reviews in Solar Physics*, 6, 2
- Norton, A. A. & Gilman, P. A. 2004, *ApJ*, 603, 348
- Parker, E. N. 1974, *ApJ*, 191, 245
- Parker, E. N. 1975, *ApJ*, 201, 494
- Parker, E. N. 1979, *Cosmical magnetic fields: Their origin and their activity* (Oxford, Clarendon Press; New York, Oxford University Press, 1979)
- Penn, M. J. & Livingston, W. 2006, *ApJ*, 649, L45
- Penn, M. J., Walton, S., Chapman, G., Ceja, J., & Plick, W. 2003, *Sol. Phys.*, 213, 55
- Peter, H. 1996, *MNRAS*, 278, 821
- Puschmann, K. G., Ruiz Cobo, B., & Martínez Pillet, V. 2010, *ApJ*, 720, 1417
- Rempel, M. 2012, *ApJ*, 750, 62
- Rempel, M. & Schlichenmaier, R. 2011, *Living Reviews In Solar Physics*, 8, 3
- Rempel, M., Schüssler, M., Cameron, R. H., & Knölker, M. 2009a, *Science*, 325, 171
- Rempel, M., Schüssler, M., & Knölker, M. 2009b, *ApJ*, 691, 640
- Rezaei, R., Schlichenmaier, R., Beck, C., & Bellot Rubio, L. R. 2006, *A&A*, 454, 975
- Riethmüller, T. L., Solanki, S. K., & Lagg, A. 2008, *ApJ*, 678, L157
- Riethmüller, T. L., Solanki, S. K., van Noort, M., & Tiwari, S. K. 2013, *A&A*, 554, A53
- Rimmele, T. 2008, *ApJ*, 672, 684
- Rimmele, T. & Marino, J. 2006, *ApJ*, 646, 593
- Rimmele, T. R. 1995a, *A&A*, 298, 260
- Rimmele, T. R. 1995b, *ApJ*, 445, 511
- Ruiz Cobo, B. & Asensio Ramos, A. 2013, *A&A*, 549, L4
- Ruiz Cobo, B. & del Toro Iniesta, J. C. 1992, *ApJ*, 398, 375
- Sánchez Almeida, J., Márquez, I., Bonet, J. A., & Domínguez Cerdeña, I. 2007, *ApJ*, 658, 1357
- Schad, T. A. 2013, *Sol. Phys.*
- Scharmer, G. B., de la Cruz Rodríguez, J., Sütterlin, P., & Henriques, V. M. J. 2013, *A&A*, 553, A63
- Scharmer, G. B. & Henriques, V. M. J. 2012, *A&A*, 540, A19
- Scharmer, G. B., Henriques, V. M. J., Kiselman, D., & de la Cruz Rodríguez, J. 2011, *Science*, 333, 316
- Scharmer, G. B. & Spruit, H. C. 2006, *A&A*, 460, 605
- Schlichenmaier, R., Jahn, K., & Schmidt, H. U. 1998a, *ApJ*, 493, L121
- Schlichenmaier, R., Jahn, K., & Schmidt, H. U. 1998b, *A&A*, 337, 897
- Schlichenmaier, R. & Schmidt, W. 2000, *A&A*, 358, 1122
- Schroeter, E. H., Soltan, D., & Wiehr, E. 1985, *Vistas in Astronomy*, 28, 519
- Schröter, E. H. 1971, in *IAU Symposium*, Vol. 43, Solar Magnetic Fields, ed. R. Howard, 167
- Schüssler, M. & Knölker, M. 2001, in *Astronomical Society of the Pacific Conference Series*, Vol. 248, Magnetic Fields Across the Hertzsprung-Russell Diagram, ed. G. Mathys, S. K. Solanki, & D. T. Wickramasinghe, 115
- Sheeley, Jr., N. R. 1972, *Sol. Phys.*, 25, 98
- Shimizu, T. 2011, *ApJ*, 738, 83
- Shimizu, T., Nagata, S., Tsuneta, S., et al. 2008, *Sol. Phys.*, 249, 221
- Sobotka, M. 1997, in *Astronomical Society of the Pacific Conference Series*, Vol. 118, 1st Advances in Solar Physics Euroconference. Advances in Physics of Sunspots, ed. B. Schmieder, J. C. del Toro Iniesta, & M. Vázquez, 155
- Sobotka, M., Brandt, P. N., & Simon, G. W. 1997, *A&A*, 328, 689
- Solanki, S. K. 1987, PhD thesis No. 8309, ETH, Zürich, The Photospheric Layers of Solar Magnetic Flux Tubes
- Solanki, S. K. 2003, *A&A Rev.*, 11, 153
- Solanki, S. K., Finsterle, W., Rüedi, I., & Livingston, W. 1999, *A&A*, 347, L27
- Solanki, S. K. & Montavon, C. A. P. 1993, *A&A*, 275, 283
- Solanki, S. K., Montavon, C. A. P., & Livingston, W. 1994, *A&A*, 283, 221

- Solanki, S. K. & Rüedi, I. 2003, *A&A*, 411, 249
- Solanki, S. K., Rüedi, I., & Livingston, W. 1992, *A&A*, 263, 339
- Solanki, S. K. & Schmidt, H. U. 1993, *A&A*, 267, 287
- Solanki, S. K., Walther, U., & Livingston, W. 1993, *A&A*, 277, 639
- Spruit, H. C., Nordlund, A., & Title, A. M. 1990, *ARA&A*, 28, 263
- Spruit, H. C. & Scharmer, G. B. 2006, *A&A*, 447, 343
- Stanchfield, II, D. C. H., Thomas, J. H., & Lites, B. W. 1997, *ApJ*, 477, 485
- Suematsu, Y., Tsuneta, S., Ichimoto, K., et al. 2008, *Sol. Phys.*, 249, 197
- Thomas, J. H. & Weiss, N. O. 2008, *Sunspots and Starspots* (Cambridge University Press)
- Title, A. M., Frank, Z. A., Shine, R. A., et al. 1993, *ApJ*, 403, 780
- Tiwari, S. K. 2012, *ApJ*, 744, 65
- Tiwari, S. K., van Noort, M., Lagg, A., & Solanki, S. K. 2013, *A&A*, 557, A25
- Tiwari, S. K., Venkatakrishnan, P., & Sankarasubramanian, K. 2009, *ApJ*, 702, L133
- Tritschler, A., Schlichenmaier, R., Bellot Rubio, L. R., et al. 2004, *A&A*, 415, 717
- Tsuneta, S., Ichimoto, K., Katsukawa, Y., et al. 2008, *Sol. Phys.*, 249, 167
- van Noort, M. 2012, *A&A*, 548, A5
- van Noort, M., Lagg, A., Tiwari, S. K., & Solanki, S. K. 2013, *A&A*, 557, A24
- Venkatakrishnan, P. & Tiwari, S. K. 2009, *ApJ*, 706, L114
- Venkatakrishnan, P. & Tiwari, S. K. 2010, *A&A*, 516, L5+
- Vögler, A., Shelyag, S., Schüssler, M., et al. 2005, *A&A*, 429, 335
- Weiss, N. O. 1991, *Geophysical and Astrophysical Fluid Dynamics*, 62, 229
- Weiss, N. O. 2002, *Astronomische Nachrichten*, 323, 371
- Weiss, N. O., Thomas, J. H., Brummell, N. H., & Tobias, S. M. 2004, *ApJ*, 600, 1073
- Westendorp Plaza, C., del Toro Iniesta, J. C., Ruiz Cobo, B., & Martínez Pillet, V. 2001a, *ApJ*, 547, 1148
- Westendorp Plaza, C., del Toro Iniesta, J. C., Ruiz Cobo, B., et al. 1997, *Nature*, 389, 47
- Westendorp Plaza, C., del Toro Iniesta, J. C., Ruiz Cobo, B., et al. 1998, *ApJ*, 494, 453
- Westendorp Plaza, C., del Toro Iniesta, J. C., Ruiz Cobo, B., et al. 2001b, *ApJ*, 547, 1130
- Wiehr, E. 2000, *Sol. Phys.*, 197, 227